Numerical Case Study of the Aerosol-Cloud-Interactions in Warm Boundary Layer Clouds over the Eastern North Atlantic with an Interactive Chemistry Module

Hsiang-He Lee[1], Xue Zheng[1], Shaoyue Qiu[1], and Yuan Wang[2]

[1]Atmospheric, Earth, and Energy Division, Lawrence Livermore National Laboratory, Livermore, CA, U.S.A.
[2]Department of Earth System Science, Stanford University, Stanford, CA, U.S.A.

Submitted to
Atmospheric Chemistry and Physics

October 2024

*Corresponding author address: Dr. Hsiang-He Lee, 7000 East Avenue, Livermore, CA, 94550, U.S.A.

E-mail: lee1061@llnl.gov

Abstract

The presence of warm boundary layer stratiform clouds over the Eastern North Atlantic (ENA) region is commonly influenced by the Azores High, especially during the summer season. To investigate comprehensive aerosol-cloud interactions, this study employs the Weather Research and Forecast model coupled with a chemistry component (WRF-Chem), incorporating aerosol chemical components that are relevant with formation of cloud condensation nuclei (CCN) and accounting for aerosol spatiotemporal variation. This study focuses on aerosol indirect effects, particularly long-range transport aerosols, in the ENA region under three different weather regimes: ridge with surface high-pressure system, post-trough with surface high-pressure system, and weak trough. The WRF-Chem simulations conducted at a near large-eddy scale offer valuable insights into the model's performance, especially regarding its high spatial resolution in capturing the mesoscale cloud features across various weather regimes. Our result shows that introducing five times more aerosols to either non-precipitating or precipitating clouds significantly increases ambient CCN numbers, resulting in varying degrees of higher LWP. The substantial aerosol-cloud interaction especially occurs in the precipitating clouds and demonstrates the LWP susceptibility to changes in CCN under different regimes. Conversely, thin, non-rain clouds at the edges of a cloud system are prone to evaporation, exhibiting an aerosol drying effect. The aerosols released during this process transition back to the accumulation mode, facilitating future activation. This dynamic behavior is not adequately represented in prescribed-aerosol simulations.

1 Introduction

Low-level stratiform clouds are predominantly generated over oceanic regions and are categorized into three main types: warm boundary layer stratiform clouds located on the eastern side of oceanic subtropical highs, stratocumulus clouds that develop over warm western boundary currents during winter cold outbreaks, and Arctic stratus (Klein and Hartmann, 1993). Warm boundary layer stratocumulus clouds, on average, blanket around 20% of the Earth's surface annually (Wood, 2012; Warren et al., 1988). Their influence on the Earth's energy balance is substantial, primarily through their ability to reflect incoming solar radiation, resulting in significant shortwave cloud radiative effects leading to a pronounced negative net radiative effect (Chen et al., 2000; Stephens and Greenwald, 1991; Hartmann et al., 1992).

Research on aerosol-cloud interactions in warm boundary layer clouds has been ongoing since the 1970s. Twomey (1974) proposed that aerosols play an important role in influencing the Earth's energy budget by serving as cloud condensation nuclei (CCN). These CCN are crucial for cloud formation. A higher concentration of CCN results in the formation of clouds with a greater number of smaller-sized cloud droplets (Twomey, 1991). These smaller droplets enhance cloud albedo, known as the first indirect effect, and inhibit precipitation formation while prolonging cloud lifetime, known as the second indirect effect (Albrecht, 1989). In addition to these indirect effects, aerosol particles have direct, semi-direct, and indirect impacts on the atmosphere's energy budgets and surface, leading to changes in atmospheric stability (Lee et al., 2008). Until now, our understanding of aerosol-cloud interactions remains incomplete. In a recent review paper, Feingold et al. (2024) highlighted that the response of cloud amount (including liquid water content, spatial coverage, and cloud persistence) to aerosol perturbations is still unclear. Both positive and negative adjustments in liquid water path (LWP) and cloud fraction (CF) have been

observed. Increases in cloud amount (positive adjustments) are linked to rain suppression, whereas enhanced evaporation of smaller droplets and entrainment feedback tend to decrease cloud amount (negative adjustments).

This study focuses on warm boundary layer stratiform clouds located on the eastern side of oceanic subtropical highs, specifically targeting the area over the Eastern North Atlantic (ENA) region, where the U.S. Department of Energy (DOE) Atmospheric Radiation Measurement (ARM) program developed a ground-based user facility in the Azores archipelago (Mather and Voyles, 2013). Long-term ground-based observations at the ARM ENA site, aircraft field campaigns near the Azores islands, and satellite retrievals over the ENA region provide comprehensive datasets for observational studies on aerosol-cloud interactions (Zheng et al., 2022; Zheng et al., 2023; Ghate et al., 2023; Qiu et al., 2024).

The presence of stratocumulus clouds over the ENA region is commonly influenced by the Azores High, also known as the Bermuda-Azores High (Rémillard and Tselioudis, 2015). This semi-permanent high-pressure system typically develops over the subtropical North Atlantic Ocean. The Azores High often brings stable and relatively dry conditions to the region, which can contribute to the formation and maintenance of stratocumulus clouds. During the summer season, the Azores High tends to strengthen and expand, leading to more persistent high-pressure conditions and often warmer, drier weather in its vicinity. Although synoptic intrusions from high latitudes are less frequent in the summer compared to the winter season (Wood et al., 2015), the ENA region still experiences synoptic variability from weak troughs during the summer months (Mechem et al., 2018; Zheng et al., 2024).

Leveraging the marine boundary layer cloud observations from the ARM ENA observatory, this study aims to study aerosol indirect effects (AIE), especially long-range transport aerosols, in the warm boundary layer clouds over the ENA region under three different synoptic regimes: ridge with surface high-pressure system, post-trough with surface high-pressure system, and weak trough (Mechem et al., 2018; Zheng et al., 2024). These regimes are chosen because the ARM site experiences northerly wind conditions during the passage of troughs. This minimizes the influence of the island effect on the observations (Ghate and Cadeddu, 2019; Zheng and Miller, 2022).

Only a few numerical studies examined aerosol-cloud interactions in marine boundary layer clouds over this region (Zhang et al., 2021; Wang et al., 2020; Kazemirad and Miller, 2020; Christensen et al., 2024). Wang et al. (2020), for example, used the Weather Research and Forecast (WRF) model with prescribed CCN profiles to simulate perturbed long-range transport aerosol concentration for two different cases of marine boundary layer (MBL) clouds. They concluded that when long-range transport aerosol plumes penetrate down into the drizzling cloud deck, the simulations show an increase in marine cloud fractions with larger water content, supporting a positive cloud amount adjustment to CCN perturbations. Christensen et al. (2024) utilized an advanced WRF configuration integrated with a Lagrangian framework to assess the effects of aerosols on developing cloud fields across 10 case study days during the ENA field campaign and got the same conclusion. However, a limitation of these studies is that they do not account for aerosol composition acting as CCN or the changes in aerosol populations following the cloud evaporation process, even though aerosol wet removal is included in their simulations.

To further investigate the impacts of realistic aerosol chemical components and aerosol spatiotemporal variation on the AIE, this study adopts the WRF model coupled with a chemistry

component (WRF-Chem) to examine the AIE in the ENA region across different synoptic regimes. A brief description of observational data and the WRF-Chem model, as well as the configuration and numerical experiments, are given in Section 2. Simulated results are discussed in Section 3, including model evaluation, model sensitivity tests, and cloud susceptibilities. The discussion and summary are provided in Section 4.

2 Methodology

2.1 Observational data

2.1.1 MERRA-2

The Modern-Era Retrospective analysis for Research and Applications, Version 2 (MERRA-2), represents the latest advancement in global atmospheric reanalysis during the satellite era. Produced by NASA's Global Modeling and Assimilation Office (GMAO), it utilizes the Goddard Earth Observing System Model (GEOS) version 5.12.4 (Molod et al., 2015). The aerosol species are from the dataset, inst3_3d_aer_Nv, which is an instantaneous 3-dimensional 3-hourly data collection in MERRA-2 (Modeling and Office, 2015). The dataset comprises assimilations of aerosol mixing ratio parameters at a native resolution of 0.5° latitude x 0.625° longitude across 72 model layers, encompassing dust, sea salt, sulfur dioxide (SO_2), sulfate (SO_4), black carbon (BC), and organic carbon (OC). The data is provided every three hours, beginning at 00:00 UTC. Based on Wang et al. (2020), we also adopt MERRA-2 to drive the WRF-Chem initial and boundary conditions for this study (see Section 2.2.2 for details).

2.1.2 Geostationary satellite retrievals (Meteosat)

Cloud properties are derived from the Spinning Enhanced Visible and Infrared Imager (SEVIRI) on Meteosat-10 and Meteosat-11, which offer a spatial resolution of 3 km at nadir and

a half-hourly temporal resolution over the ENA region. These SEVIRI cloud products are generated using the Satellite ClOud and Radiation Property retrieval System (SatCORPS) algorithms (Painemal et al., 2021). These methods, developed by the Clouds and Earth's Radiant Energy System (CERES) project, are specifically tailored to support ARM ground-based observation sites (Minnis et al., 2011; Minnis et al., 2021). Specifically, this study adopts cloud fraction for all clouds as the observational reference over the ENA region. The adopted data have been specifically processed (e.g., solar zenith angle, cloud optical thickness, and cloud labels) and averaged to 25 km × 25 km (Qiu et al., 2024).

2.1.3 Aircraft observation

The U.S. DOE ARM Aerosol and Cloud Experiments in the Eastern North Atlantic (ACE-ENA) aircraft field campaign near the Azores islands provided extensive observations of the vertical distributions of aerosol and cloud properties (Wang et al., 2022). Intensive operational periods (IOPs) of the ACE-ENA took place in late June and July 2017, as well as January to February 2018. During the 2017 summer IOP, the ARM Aerial Facility's (AAF) Gulfstream-159 (G-1) aircraft delivered precise measurements of aerosol size distribution, total aerosol number concentration, and chemical constituents both below and above cloud layers. SO_4 and OC mass concentrations were measured using the Aerodyne High-Resolution Time-of-Flight Aerosol Mass Spectrometer (HR-ToF-AMS), while refractory BC was measured by the Single Particle Soot Photometer (SP2). Detailed information about each instrument is available on the ARM website (https://www.arm.gov/research/campaigns/aaf2017ace-ena). In this study, aircraft measurements of SO_4, OC, and BC from 19 July 2017, are utilized to assess the simulated aerosol vertical profile. However, uncertainties arising from the measurements and spatiotemporal sampling strategies may hinder direct comparisons of absolute values between the observations and modeled results.

2.1.4 ARM ground-based observations

The DOE ARM ground-based instruments deployed on Graciosa Island in the Azores archipelago provide comprehensive measurement of aerosols, clouds, radiation, atmospheric boundary layer, and other atmospheric properties. In this study, LWP is retrieved from the brightness temperature measured by the microwave radiometer (MWR) at 23.8 and 31.4 GHz (Liljegren et al., 2001) and used for model evaluation. The temperature and moisture profiles are from the interpolated sonde data, derived from the radiosonde measurement.

2.2 The model

2.2.1 WRF-Chem

The Weather Research and Forecasting (WRF) model version 4.4.2 (Skamarock et al., 2021) coupled with a chemistry component (WRF-Chem) (Grell et al., 2005) is used in this study. The standard WRF-Chem permits the simulation of the combined direct, indirect, and semi-direct effects of aerosols (Grell et al., 2005; Fast et al., 2006; Chapman et al., 2009). WRF-Chem version 4.4.2 has sophisticated packages to represent chemistry processes (i.e., gas-phase reaction, gas-to-particle conversion, coagulation, etc.) and aerosol size and composition (Binkowski and Shankar, 1995). In this study, the Regional Acid Deposition Model version 2 (RADM2) photochemical mechanism (Stockwell et al., 1997) is integrated alongside the Modal Aerosol Dynamics Model for Europe (MADE) and the Secondary Organic Aerosol Model (SORGAM) (Ackermann et al., 1998; Schell et al., 2001) to simulate atmospheric chemistry and the evolution of anthropogenic aerosols. MADE/SORGAM adopts a modal approach to represent the aerosol size distribution, predicting mass and number concentrations across three aerosol modes (Aiken, accumulation, and coarse). MADE/SORGAM has inorganic, organic, and secondary organic aerosols and contain aerosol formation processes including nucleation, condensation, and coagulation. WRF-Chem

198 tracks the number of particles and the mass of chemical compounds (e.g., SO_4^{2-}, NH_4^+, NO_3^-, Na^+,
199 Cl^- etc.) in each aerosol mode, including both interstitial aerosols and aerosols present in liquid
200 water (the sum of cloud and rain), as prognostic variables.

201 The size, composition, and mixing state of aerosols significantly influence their capability
202 to activate as CCN (Zaveri et al., 2010). A physically based aerosol activation parameterization
203 scheme has been developed for climate models to simulate CCN concentration accurately and
204 efficiently (Abdul-Razzak and Ghan, 2000). This aerosol activation parameterization was initially
205 designed for a single aerosol type with a lognormal size distribution. Then, they expanded this
206 parameterization to accommodate multiple externally mixed lognormal modes, with each mode
207 consisting of both soluble and insoluble materials internally mixed. However, WRF-Chem
208 (MADE/SORGAM) chemistry package adopts this global internal mixing assumption, where all
209 particles within a log-normal mode within the same grid cell are instantly combined, resulting in
210 the same chemical composition. This instantaneous internal mixing assumption modifies the
211 optical and chemical characteristics of particles in WRF-Chem simulations, potentially impacting
212 aerosol-cloud interactions, such as aerosol activation as CCN (Zhang et al., 2014).

213 ### 2.2.2 The configuration

214 Our focus in this study is to examinate aerosol-cloud interactions close to the scale of large-
215 eddy simulation (LES) over the ARM ENA site. We use WRF-Chem with a full chemistry
216 package involving sophisticated gaseous and aqueous chemical processing calculations and dry
217 and wet depositions. The numerical simulations are employed with 4 domains consisting of 4
218 horizontal resolutions of 5 km, 1.67 km, 0.56 km, and 0.19 km, respectively (Fig. 1), with one-
219 way nesting. There are 550 × 530 grids for D1, 451 × 430 grids for D2, 553 × 532 grids for D3,
220 and 553 × 532 grids for D4. The domain size of domain 4 is about 1 degree which is similar to

the spacing resolution of global climate models. Seventy-five vertically staggered layers are stretched to have a higher resolution near the surface based on a terrain-following pressure coordinate system. With this setup, the model has roughly 24 model layers in the boundary layer (~2000 m). The time step is 30 and 10 seconds for advection and physics calculation for domains 1 and 2, respectively. The nesting inner domains 3 and 4 have the time step of 3 seconds and 1 second, respectively. The physics schemes adopted in the simulations are listed in Table 1. The initial and boundary meteorological conditions are taken from ERA5, developed by the Copernicus Climate Change Service (C3S) at ECMWF (European Centre for Medium-Range Weather), stands as the fifth generation of ECMWF atmospheric reanalysis, spanning from January 1940 to the present day (Hersbach et al., 2023). This comprehensive dataset offers hourly estimates of numerous atmospheric, land, and oceanic climate variables, covering the entirety of Earth on a 31 km grid. The atmospheric component is resolved using 137 levels, spanning from the surface up to 80 km in height.

The computational expense of conducting a 4-domain WRF-Chem simulation, particularly with LES resolution, is exceedingly high. To mitigate this, we execute WRF solely for the two outer domains (d01 and d02), leveraging the WRF downscaling module (ndown) (Skamarock et al., 2008) to generate meteorological initial and boundary conditions for domain 3. As a result, we only need to perform WRF-Chem simulations for the two inner domains (d03 and d04), leading to an almost 50% reduction in total computational costs (compared to the original 4-domain run, which had a throughput of 4 hours per day using 1080 cores). It is important to note that a high temporal frequency for domain 3 boundary conditions is essential due to its fine horizontal resolution (0.56 km). In this context, we update the boundary condition every 5 minutes for domain 3.

To enhance the realism of aerosol mass simulation in remote marine regions, such as the ENA site, we account for major aerosol species (BC, OC, and SO_4), as well as SO_2, from MERRA-2 into the boundary conditions of domain 3. Aerosols in the initial condition are introduced into the restart file (wrfrst) following a one-hour initial run, rather than in the initial condition file (wrfinput), to address certain numerical challenges. According to the emission setup for MADE/SORGAM, we assume that the Aiken mode and the accumulation mode account for 20% and 80% of the aerosol mass (BC and OC), respectively (Tuccella et al., 2012). Conversely, for SO_4, 80% is allocated to the Aiken mode and 20% to the accumulation mode, reflecting the faster growth rate of SO_4 and a longer duration of growth from the domain 3 boundary. Because MERRA-2 only provides aerosol mass, the aerosol number concentrations for different aerosol species are estimated with the density assumption of BC (1.7 g cm^{-3}), OC (1.0 g cm^{-3}) and SO_4 (1.77 g cm^{-3}) based on Liu et al. (2012). Aerosol optical depth retrieved from satellite remote sensing can offer valuable information for comparison; however, it may be subject to high bias in our study cases due to cloud cover.

It is common to consider that the ENA region is an unpolluted area because it is far away from the anthropogenic pollution sources. Besides long-range transport aerosols, two local aerosol sources, dimethyl sulfide (DMS) and sea salts, are also important for the aerosol budget. Kazil et al. (2011) pointed that the observed DMS flux from the ocean in the VOCALS-REx field campaign over the Southeast Pacific can support a nucleation source of aerosol. DMS oxidation by nitrate (NO_3) produces SO_2 and then increases SO_4 concentration (Toon et al., 1987). Since we adapted SO_2 and SO_4 concentration from MERRA-2 in the initial and boundary conditions, we did not double count DMS emissions in our simulations. As a result, chemical species emissions, except for sea salt, are excluded from the simulations. The emission of sea salt particles is parameterized

using the method outlined by Clarke et al. (2006) in WRF-Chem. Sea salt emissions are driven by surface wind speed. The simulated surface wind speed aligns closely with ERA-5 data; however, the sea salt concentration is only one-third of the value found in the MERRA-2 analysis. To improve the alignment with the sea salt aerosol concentration observed in the MERRA-2 reanalysis, we adjust the parameter factor for sea salt emissions to three times the original estimate (further comparison can be found in Section 3).

2.3 Study cases and numerical experiment design

We select three specific study cases to assess the impact of long-range transport aerosols on warm boundary layer clouds, with each case representing a typical meteorological regime observed over the ENA site. The first case, dated 1 July 2016, exhibits the formation of overcast stratocumulus clouds (Fig. 2a) within a meteorological regime characterized by a ridge system in the free troposphere and a high-pressure system near the surface (Fig. 2d). Predominant northwesterly and northerly winds in the area of the ARM ENA site coincide with the presence of long-range transport aerosols, commonly found along the periphery of the high surface pressure system (Logan et al., 2014; Gallo et al., 2023).

The second case on 19 July 2017 is a stratocumulus cloud case (Fig. 2b) within a post-trough regime featuring a high surface pressure under the influence of a trough system (Fig. 2e). Following the trough passage, robust northwesterly winds facilitated the influx of long-range transport aerosols into the region, which then shifted to northerly winds as the trough moved away. Because the ACE-ENA aircraft field campaign intensive operations period (IOP) was during this time, aircraft aerosol observational data can be used to evaluate the model performance for this case.

Finally, the third case, dated 23 August 2019, occurred during a period of weak trough activity (Fig. 2f). Here, we noted the presence of broken, thicker stratocumulus clouds, often accompanied by deeper cloud formations (Fig. 2c). Long-range transport aerosols were again observed, primarily carried by northwesterly and northerly winds, albeit with weaker surface wind speeds compared to the preceding two cases.

All simulations start at 12 UTC on the preceding day of the study case, spanning a duration of 36 hours, with the initial 12 hours dedicated to spin-up. Again, aerosols in the initial condition are introduced into the restart file after one-hour initial run (i.e., 13 UTC). The three aforementioned cases, labeled as control cases (20160701_control, 20170719_control, and 20190823_control), are utilized to examine the behavior of warm boundary layer clouds under diverse meteorological conditions. Additionally, we formulated three perturbed cases (20160701_perturbed, 20170719_perturbed, and 20190823_perturbed) by amplifying aerosol concentrations in both initial and boundary conditions, as well as sea salt emissions, by a factor of five relative to each control case. These control cases represent clean conditions, with near-surface CCN concentrations below 100 cm^{-3} at the ARM ENA site. A comparison between the control and perturbed cases elucidates the sensitivity of warm boundary layer clouds to aerosol enhancements under varying meteorological conditions, thereby contributing to a deeper understanding of cloud microphysics processes under varying atmospheric dynamics.

3 Results

3.1 Model evaluation

3.1.1 Meteorological conditions

Figures 2g, 2h, and 2i display the model-simulated LWP in the control runs over domain 3 and 4. The modeled LWP is calculated in-cloud LWP only. The simulations with fine spatial

resolution effectively capture synoptic frontal systems and cloud features, particularly when compared to the cloud images from the Meteosat satellite (Figs. 2a, 2b, and 2c). Thin, uniform stratocumulus clouds on 1 July 2016 are simulated in 20160701_control, while the solid stratocumulus and frontal system on 19 July 2017 are also well captured in 20170719_control. Broken stratocumulus clouds on 23 August 2019 are reproduced in the simulation of 20190823_control. Figures 2j, 2k, and 2l display the model-simulated LWP in the perturbed runs. The overcast stratocumulus clouds are simulated better in 20160701_perturbed (Fig. 2j), which more accurately reflects reality.

The control runs serve as a basis for comparing the boundary layer structure against the interpolated soundings obtained from the ARM ENA site. Figure 3 depicts the comparison, showing the simulated air temperature aligning closely with the observed values. However, on 1 July 2016, the model (20160701_control) displays a warm bias in capturing the temperature inversion (Figs. 3a and 3b), with the simulated inversion layer situated approximately 200-300 m lower than observed during the whole study period. Potential temperature and relative humidity have consistent performance as illustrated in Figs. S1b and S2b, respectively. While the model indicates high relative humidity (> 90%) within 1000 m, observations show this extending up to ~1200 m.

For the 19 July 2017 case, the model (20170719_control) successfully represents the diurnal cycle of temperature vertical gradient within 1000 m height. However, compared to observations, the model does not catch the inversion at 1500 m height near the noon time and shows a warm bias in the model's simulated temperature (Figs. 3c and 3d). The model simulation also tends to depict drier conditions in the evening compared to the observation (Figs. S3c and S3d).

On 23 August 2019, characterized by a weak trough regime and higher boundary layer height, the simulation of 20190823_control accurately captures warm and moist air advection in the morning but has difficulty in maintaining fidelity in the late afternoon. Notably, the lower troposphere becomes excessively warm and dry after 17 Z local time compared to observations (Figs. 3e, 3f, S2e, S2f, S3e, and S3f).

In general, all simulations effectively capture large-scale conditions and cloud features (Fig. 2) across different synoptic regimes but do not accurately represent temperature inversions and air advection patterns. Discrepancies are noted in the simulated boundary layer height, which is lower, and the inversion is weaker than actual observations. Furthermore, the discrepancies tend to increase in the later stage of simulation.

3.1.2 Aerosol evolution

As mentioned in Section 2.2.2, we incorporate major aerosol species (BC, OC, and SO_4), from MERRA-2 into the domain 3 initial (in the restart file at 13 UTC) and boundary conditions to enhance the realism of aerosol simulation. Figure 4 shows time-series SO_4 vertical profiles from both MERRA-2 and WRF-Chem for three study cases. Here, we demonstrate the time evolution of SO_4. This species is the main aerosol component among the three introduced aerosol species, about 60~80% of total aerosol mass, in the initial conditions.

Compared to the MERRA-2 data, 20160701_control well captures the long-range transport SO_4 between 1000 m and 2000 m, which is above the cloud deck, on 1 July 2016 (Figs. 4a and 4b). The observed high BC and OC are also concentrated in this layer (Figs. S4a and S5a), as well as simulated ones (Figs. S4b and S5b). Figures 4c and 4e show two MERRA-2 time-series vertical distributions of SO_4 on 19 July 2017 and 23 August 2019, both showing low-altitude (below 1500 m) aerosol plumes. On 19 July 2017, the concentrations of BC and OC showed two peaks – one

near the surface and another above 1500 m in the free troposphere (Figs. S4c and S5c). This pattern indicates the presence of a biomass-burning signature in the plume on that day (Wang et al., 2020). While the simulation of 20170719_control did not capture the near surface BC, OC, and SO_4 concentration after 11 Z local time on 19 July 2017 (Figs. S4d, S5d, and 4d). It is because in the case of the post-tough regime, the wind direction changes from northwesterly to northerly when the trough moved away, and the aerosol plume in domain 3 did not propagate into domain 4 when the wind direction changed (figure not shown). However, the simulation of 20170719_control still captures the BC and OC plumes in the free troposphere (above 2000 m height) (Figs. S4d and S5d).

Aircraft observations during ACE-ENA provide more accurate depictions of aerosol vertical distribution and aerosol layer heights, with differentiation of aerosol type. Figure 5a shows the vertical distribution of aerosol mass concentrations averaged over the flights on 19 July 2017. BC, OC and SO_4 all increase with height above clouds (~1000 m), indicating downward propagation of aerosol plumes and possible interaction with MBL clouds (600 – 1000 m). Here, we also see that high SO_4 in the free troposphere, similar to MERRA-2, but the model underestimates the OC concentration in the free troposphere. On the other hand, within the MBL, there is a much higher concentration of SO_4 in the MBL than those of BC and OC in the observations. This phenomenon is also captured by the WRF-Chem simulation (Fig. 5b), but the model did not capture the magnitude of the SO_4 concentration.

Similarly, for the case of 20190823, within the low boundary layer, there is a much higher concentration of SO_4 in the low boundary layer (Fig. 4e). After the noon time on 23 August 2019, BC and OC show both high-altitude plumes and low-altitude plumes approaching into the domain, which indicate potentially two different aerosol sources (Figs. S4e and S5e). Again, while the

simulation of 20190823_control well captures the time evolution of aerosol plume, the boundary of high-altitude plumes and low-altitude plumes appears 300 m lower in the simulations (~600 m in altitude; Figs. S4f and S5f) compared to the observations (~900 m in altitude).

Sea salt particles serve as an important source of CCN over the ocean, particularly in unpolluted conditions. However, due to their larger particle size, sea salt particles tend to accumulate near the ocean surface and are swiftly removed by dry deposition and sedimentation processes (Chin et al., 2002). The simulation of 20160701_control (Figs. S6a and S6b) accurately reproduces sea salt concentrations, both in magnitude and vertical distribution, consistent with observations, same as the case of 20170719 (Figs. S6c and S6d). Nevertheless, the model encounters difficulties in simulating sea salt concentrations for the case of 23 August 2019 (Figs. S5e and S5f), corresponding to a weak-trough system (Fig. 2c). Although the simulated surface wind speed matches well with ERA-5 (Fig. S7), the underestimation of sea salt concentrations may be attributed to limitations in the emission parameterization, which is overly reliant on surface wind speed (Gong, 2003).

3.1.3 Cloud properties

In Fig. 6, we observe a comparison between the simulated results and observations of LWP and CF at different spatial scales (4 km- and domain-average, respectively) to leverage the spatiotemporal advantages offered by both sets of observations. The ARM ground-based instrument recorded an LWP of over 400 g m^{-2} during the nighttime with drizzle droplets reaching to the surface on 1 July 2016 (Fig. 6a). As the sunrise (around 6 Z local time), the LWP decreases to a range of about 100 g m^{-2} and then increases again to 600 g m^{-2} after 21 Z local time.

To compare with the ARM ground-based observations, the WRF-Chem simulated result is averaged over 20 × 20 grids centered on the Azores, which corresponds to an approximate resolution of 4 km (Fig. 6a). Overall, the control run generates a thin cloud layer with an underestimated LWP during the nighttime, capturing only 10-20% of the observed LWP. The simulated clouds are more consistent with the observations during the daytime, especially in the perturbed run. However, it is important to note that the LWP retrieved by MWR experiences significant uncertainties during drizzling or precipitating conditions. This is primarily due to the scattering effects of large raindrops and raindrops accumulating on the instrument's radome, which can result in an overestimation of LWP (Tian et al., 2019; Cadeddu et al., 2020).

Figure 6b depicts the comparison of CF between observations and WRF-Chem. The CF values obtained from Meteosat are close to 1, indicating a solid cloud field. In contrast, the CF simulated by 20160701_control range between 0.5 and 0.9 on a domain-averaged scale. Similar to the LWP results, the simulated CFs from 20160701_control exhibit a diurnal cycle, with higher values during the nighttime and lower values during the daytime. Due to the thinner clouds simulated in 20160701_control based on LWP, the modeled CF is 40-60% lower than the observation in the afternoon, indicating that clouds dissipate more quickly in the control run. Conversely, the 20160701_perturbed scenario demonstrates improved performance in both LWP and CF. This indicates that the 20160701 case is sensitive to aerosol variations, with the CCN number being too low in the control run.

Compared to a ridge system like the case of 20160701, the WRF-Chem model has difficulty in capturing the warm boundary layer clouds under a regime characterized by a post-trough system (20170719) or a weak trough system (20190823). Compared to the observations, the simulated LWP in 20170719_control is about 30% of the observed value (Fig. 6c. In contrast,

the simulated CF performs better, reaching about 75% of the observed value (Fig. 6d). The discrepancy between the modeled results and observations may arise from delayed moisture transfer from the outer domain or insufficient vertical resolution. In this instance, the cloud systems move quickly under the post-trough weather regime. A 5-minute moisture input from the boundary condition using WRF downscaling (ndown) may not be sufficient to transport moisture into the inner domain, making it difficult for the model to develop thicker marine stratocumulus clouds, especially for such high spacing resolution. On the other hand, in another ongoing project, we increased the vertical layers to 99, which is to double vertical layers below 2km. However, the test with 99 levels only slightly improves the cloud cover and LWP. The estimated LWP susceptibility shows little to no change. The insignificant improvement indicates even higher resolution is needed to fully simulate the cloud processes near the sharp boundary layer inversion for these solid stratocumulus cloud layer. Another possible reason is that the 6th Order Horizontal Diffusion used in the study (diff_6th_opt = 2) rapidly dissipates marine stratiform clouds, especially in the high spacing resolution (Knievel et al., 2007). It is worth noting that Christensen et al. (2024) conducted sensitivity tests using various shallow cumulus and microphysics schemes, and the different combinations of these schemes had a substantial impact on the simulated cloud amount as well.

Moving to the case of 20190823, overall, compared to the observations, the control run captures LWP and CF slightly better, especially in the domain-averaged scale (Figs. 6e and 6f). Based on the LWP observed from ARM, there are two systems passing in the area, one between 5 Z to 13 Z local time and the other between 17 Z to 22 Z local time on 23 August 2019 (high ARM LWP in Fig. 6e). The simulation of 20190823_control captures the first system, but slightly underestimates LWP; however, the model misses the second system. The model simulated CFs

448 also match well with Meteosat (Fig. 6f). Only after 17 Z, the model misses catching the second
449 system. The CFs drops 50 – 70 % compared to the observations.

450 The underestimation of LWP and CF in model simulations leads to insufficient longwave
451 cooling at the cloud top. This reduced cooling weakens cloud-top entrainment, resulting in a less
452 pronounced boundary layer inversion and a shallower boundary layer height identified in Section
453 3.1.1. This creates a negative feedback loop, where the initial inaccuracies in cloud properties
454 affect boundary layer dynamics (Zheng et al., 2021). On the other hand, in the perturbed runs, the
455 results show an adjustment in the amounts of LWP and CF, aligning more closely with the
456 observations. This suggests that the CCN number is underestimated in the control runs (more
457 discussion in Section 3.3). The model's response to aerosol changes highlights its capability for
458 studying aerosol-cloud interactions.

459 3.2 Aerosol composition and activation

460 The advantage of utilizing WRF-Chem to investigate aerosol-cloud interactions stems from
461 its capability to simulate the spatiotemporal distribution of CCN. This modeling is based on
462 various aerosol components and their sizes, as well as their dynamic responses to wet removal
463 processes associated with clouds and precipitation. In traditional simulations that rely on fixed or
464 prescribed aerosol distributions, accurately representing these factors can be particularly
465 challenging. WRF-Chem, however, allows for a more nuanced understanding by dynamically
466 modeling how aerosol populations evolve over time, especially after cloud evaporation processes.
467 During the evaporation process, the reduction in cloud water can lead to a re-entrainment of
468 aerosols back into the atmosphere, altering their concentration and properties. This change can
469 affect subsequent cloud formation and precipitation patterns, highlighting the importance of
470 capturing these interactions for reliable predictions.

In this section, we concentrate on aerosol activation, considering its size and chemical composition across three different cases. The following section will discuss the aerosol indirect effect and how changes in cloud properties feedback into the aerosol population and its activation capability.

In Fig. 7a, the blue solid line and blue dashed line represent the vertical profiles of total aerosol number concentration (including Aiken mode and accumulation mode) and aerosol number concentration of the Aiken mode, respectively. These profiles are averaged over domain 4 on 1 July 2016. The environment shown in the figure is characterized by its cleanliness, with a total aerosol number concentration below the cloud top (approximately 1000 m in height) measuring less than 300 cm^{-3}. In the 20160701_control simulation, the total aerosol number is low, and approximately 70% of the total aerosol numbers belong to the Aiken mode. According to the study conducted by Mccoy et al. (2024), which utilized aerosol number concentration measurements from ARM airborne observations on 15 July 2017, it was found that the ratio of the Aiken mode to the total aerosol number was approximately 50-60% within an altitude of 1000 m. Compared to this observational analysis, our simulations generate an overabundance of small-sized aerosols, which result in a low concentration of CCN. This discrepancy arises from the assumptions made when constructing the aerosol initial and boundary conditions (80% for Aiken mode and 20% for accumulation mode SO_4).

The CCN calculation presented in Fig. 7a is based on the Köhler theory, which considers both the aerosol size (curvature effect) and the chemical composition (solution effect) to estimate the theoretical CCN number concentration at different supersaturations. Below 1.0% supersaturation, the CCN number concentration is found to be 42% of the total number of aerosol number (could be estimated from 100% of accumulation mode and 16% of Aiken mode) (Fig.

S8a). In the simulation of 20160701_control, the CCN number concentration below 0.2% (0.5%) supersaturation is only 11% (25%) of the total aerosol number, which is lower than the observations reported in Wang et al. (2020), where the observed CCN number concentration under 0.35% supersaturation was approximately 25% of the total aerosol number. Even though SO_4 is the dominant chemical component, accounting for nearly 50% (as shown in Figs. 8b and 8c), the presence of an excessive number of Aiken mode aerosols may be the primary reason for the low activation rate. The curvature effect caused by these Aiken mode aerosols hinders their ability to act as CCN effectively.

In the simulation of 20170719_control, the most aerosols are within a height of 1000 m, which is also the cloud layer (Fig. 7d). The average aerosol number concentration across the entire domain is measured to be 1286 cm^{-3} within a height of 2000 m and the Aiken mode is 80% of the total aerosol number in this case. The chemical composition of aerosols in the 20170719_control mainly is SO_4 with the other species exhibiting lower concentrations (Figs. 7e and 7f). This variation in vertical distribution leads to more aerosols being activated under the cloud top at a height of 1500 m. This is attributed to the presence of a peak value of accumulation mode aerosols and SO_4 at this height.

Because of the high number concentration of simulated Aiken mode aerosols, overall, the activation rate is low. Below 1.0% supersaturation, the CCN number concentration is estimated to be 25% of the total aerosol number. This could be a result of 100% of the accumulation mode aerosols and 7% of the Aiken mode aerosols contributing to the CCN population (Fig. S8c). The CCN number concentration below 0.2% (0.5%) supersaturation is only 4% (12%) of the total aerosol number.

Among the three cases studied, the case of 20190823 stands out as the most polluted case, but the aerosol component and vertical distribution are close to the case of 20170719 (Figs. 7c and 7i). The average aerosol number concentration across the entire domain is measured to be 1850 cm^{-3} within a height of 2000 m. The Aiken mode aerosols are also high and contribute to more than 75% of the total aerosol number in this case (Figs. 7g and S8e). The large SO_4 species concentration also leads to more aerosols being activated under the cloud top at a height of 2000 m. The CCN number concentration below 0.2% (0.5%) supersaturation is only 6% (17%) of the total aerosol number, slightly better than the case of 20170719.

The cloud droplet numbers observed in the three cases fall within the range of CCN numbers below 0.1% and 0.2% supersaturation. Therefore, in the subsequent sections, we utilize the CCN number concentration below 0.2% supersaturation as a representative of the CCN activation rate.

3.3 Cloud responses to aerosol perturbations

Figure 8 illustrates the comparison of time series profiles of cloud water content (CWC) and CCN number concentration below 0.2% supersaturation between the control runs and perturbed runs. This figure also demonstrates the CCN spatiotemporal variation in our simulations. Specifically, for the case of 20160701, it is evident that the CWC in 20160701_perturbed exhibits a positive response to increased CCN compared to the CWC in 20160701_control. This result aligns with most WRF studies that use fixed or prescribed CCN numbers to investigate aerosol-cloud interactions (Wang et al., 2020; Christensen et al., 2024).

Echoing the insufficient longwave cooling at the cloud top due to the underestimation of LWP and CF in model simulations discussed in Section 3.1.3, Terai et al. (2014) also observed

weak cloud-top entrainment in their study of five pockets of open cells, using aircraft data from the VOCALS Regional Experiment (VOCALS-REx). Their research indicated that clouds tend to break up easily in the absence of aerosols, characteristic of a pristine environment. Consistent with their findings, our study demonstrates that in-cloud collision–coalescence processes effectively remove aerosols, particularly because of the wider range of cloud droplet sizes present in a clean environment (i.e., the control runs) (Table 2). Even in the control run for 20160701, our results indicate that broken open cell clouds in a pristine environment struggle to develop into closed clouds.

Figure 9a depicts the time series of domain-averaged LWP, encompassing both cloud and rain, and CCN number concentration below 0.2% supersaturation for both the 20160701_control and 20160701_perturbed cases. This visualization provides a quantitative representation of the change in CCN number concentration, which increases from a mean value of 32.52 cm^{-3} in the control run to 127.68 cm^{-3} in the perturbed run, approximately four times higher than the control run. Because we want to avoid counting high CCN number concentration above cloud top which do not readily become cloud droplets, the CCN number concentration is averaged from the surface up to the height of 1000 m (Wang et al., 2020).

The LWP in the 20160701_control case exhibits a domain mean value of 64.88 g m^{-2}, which subsequently increases to 123.27 g m^{-2} in the 20160701_perturbed case. As mentioned in Section 3.1, the LWP for the 20160701 case follows a diurnal cycle, with higher values during nighttime and lower values during daytime. This diurnal cycle is also observed in the perturbed simulation, with the larger differences in CCN and LWP between the control run and perturbed run during nighttime (Fig. 9a).

After increasing the aerosol concentration, the cloud droplet number in the 20160701_perturbed run demonstrates similar responses. In the 20160701_control case, the domain mean value of the cloud droplet number is 14.03 cm^{-3}, which subsequently increases to 45.52 cm^{-3} in the 20160701_perturbed case. As the cloud droplet number increases, the cloud radius decreases from 12.23 μm in the control run to 10.08 μm in the perturbed case.

The case of 20170719 represents a post-trough weather regime, and Fig. 8c illustrates the passage of a frontal system in the area after 8 Z local time on that day. In the 20170719_perturbed simulation, the CWC increases following the system's passage (Fig. 8d) compared to the CWC in the 20170719_control run. Additionally, the ambient CCN number in the perturbed run is also higher. The time variation of CCN concentration in Fig. 9c shows elevated CCN numbers before and after the system enters the domain. In the 20170719_control case, the domain mean value of CCN number concentration is 60.51 cm^{-3}, which subsequently increases to 253.51 cm^{-3} in the 20170719_perturbed case. The domain-averaged LWP also exhibits an increase, rising from 59.31 g m^{-2} in the 20170719_control run to 74.07 g m^{-2} in the 20170719_perturbed case. Notably, this change primarily occurs after the passage of the frontal system.

The cloud droplet number consistently shows higher values in the perturbed case (Fig. 9d), and this pattern is similar to the difference in CCN between the two runs of 20170719 (Fig. 9c). In the 20170719_control case, the domain mean value of cloud droplet number is 20.70 cm^{-3}, while the value is 56.09 cm^{-3} in the perturbed case. When the cloud droplet number increases in the perturbed run, the cloud radius decreases from 9.90 μm in the control run to 7.49 μm in the perturbed case. This reduction in cloud radius is even smaller than the cloud radius observed in the case of 20160701.

582 The case of 20190823 is similar to the case of 20170719, but it represents a weak trough
583 weather regime. Figure 8e also illustrates the passage of a cloud system in the area between 5 Z
584 to 17 Z local time on 23 August 2019, and the CWC in the perturbed run increases during this
585 period. Quantitatively, in the 20190823_control case, the domain mean value of CCN number
586 concentration is 124.32 cm^{-3}, which subsequently increases to 475.37 cm^{-3} in the
587 20190823_perturbed case, which is also about three times higher. The domain-averaged LWP
588 also exhibits an increase, rising from 48.92 g m^{-2} in the 20190823_control run to 58.53 g m^{-2} in
589 the 20190823_perturbed case.

590 Differing from the case of 20170719, the frontal system moved away from the study
591 domain after the noontime, the differences of CCN number or cloud droplet number between the
592 control and perturbed runs becomes even more pronounced after the system (Figs. 9e and 9f). It
593 is because aerosols are transported to the area following the frontal system (Fig. 4f) and then more
594 aerosols activated as CCN. In the 20190823_control case, the domain mean value of cloud droplet
595 number is 33.94 cm^{-3}, while the value is 79.97 cm^{-3} in the perturbed case. When the cloud droplet
596 number increases in the perturbed run, the cloud radius decreases from 8.51 μm in the control run
597 to 6.45 μm in the perturbed case. This reduction in cloud radius is similar to the cloud radius
598 observed in the case of 20170719.

599 We observe that large aerosol-induced LWP occurs during the periods of rainfall (Fig. S9).
600 To accurately quantify the differences, we calculate the average LWP over approximately 25 km
601 of domain 4. This results in 16 averaged grids per output file, with each file generated every 10
602 minutes. This averaging process is based on Arola et al. (2022) and Zhou and Feingold (2023) to
603 avoid the impact of heterogeneity and co-variability on the results. Specifically, we aggregate the

simulation grids with a spacing resolution of approximately 190 m to form a larger grid of around 25 km for each 10-minute simulation output, as shown in Fig. S10a.

Table 2 presents the 10-minute mean and standard deviation of several variables, including CCN, LWP, cloud droplet number (Nc), cloud radius (Re), and rainfall intensity (RI), across three study cases. The classification of "rain" and "non-rain" is based on the RI (unit: mm hr^{-1}) on the averaged grid. Specifically, a grid is considered as "rain" if the RI is greater than zero. In the control cases, the averaged CCN number is 73.07 cm^{-3}, and the corresponding LWP is 53.17 g m^{-2}. However, in the perturbed cases, the CCN number increases approximately threefold, reaching 218.21 cm^{-3}, and the LWP increases by 49% to 79.25 g m^{-2}. The introduction of additional aerosols in the perturbed cases also leads to a significant increase in the Nc number, from 22.68 cm^{-3} in the control cases to 59.74 cm^{-3} in the perturbed cases. Consequently, the Re decreases by 21% from 9.97 μm to 7.83 μm, and the RI decreases by 11% from 0.009 mm hr^{-1} to 0.008 mm hr^{-1}.

To investigate the interaction between aerosols and clouds, we analyze the results separately for rain and non-rain grids. In both the control and perturbed cases, we observe that the CCN number within 1000 m is lower in the rain grids compared to the non-rain grids, primarily due to the washout effect caused by rainfall. Additionally, the LWP over the rain grids is generally higher than that over the non-rain grids. Furthermore, when comparing the control and perturbed cases, we find that the LWP over the rain grids increases by 57% from 58.57 g m^{-2} to 91.81 g m^{-2}. In contrast, the LWP over the non-rain grids only increases by 28% (Table 2). This difference can be attributed to the conversion of cloud droplets to raindrops through processes like autoconversion and collection, which occurs more prominently over the rain grids. We also observe that in the non-rain grids, especially at the cloud edges (or low LWP), the perturbed cases reveal an increased presence of small cloud droplets. This abundance of smaller droplets facilitates evaporation,

627 resulting in a reduced LWP (e.g., clouds in the bottom right corner of Figs. S10a and S10b).
628 Consequently, Nc over the rain grids is lower compared to Nc over the non-rain grids. Moreover,
629 when introducing aerosols in the perturbed runs, the results over the rain grids exhibit larger cloud
630 drops and a wider radius spectrum compared to the results over the non-rain grids. This suggests
631 that the presence of aerosols has a more pronounced effect on cloud properties within the rain
632 grids.

633 Zheng et al. (2022) conducted a study on the aerosol-cloud interaction using ground-based
634 measurements from the ARM program, focusing on the influence of environmental variables.
635 Their findings revealed that when there is ample water vapor and low CCN loading, the active
636 coalescence process leads to a broader size distribution of cloud droplets, resulting in an increase
637 in cloud droplet radius. On the other hand, when there is enhanced activation of CCN and
638 condensational growth of cloud droplets due to higher CCN loading below the cloud, the cloud
639 droplet radius decreases. This combined effect signifies an intensified aerosol-cloud interaction,
640 leading to a broad range of cloud droplet radii. The simulated results in our study, specifically
641 over the rain grids where a sufficient water vapor environment is considered, demonstrate a
642 significant aerosol-cloud interaction, where increased CCN introduces more newly converted
643 droplets, resulting in a broad range of cloud droplet radii.

644 Since we utilize a comprehensive aerosol module in WRF-Chem to examine aerosol-cloud
645 interactions, we are able to explore how changes in cloud properties, driven by increased CCN,
646 affect aerosol concentrations. For example, in the post-trough regime (20170917 case) and the
647 weak trough regime (20190823 case), we observe that the cloud structure exhibits more open-cell
648 stratocumulus clouds (Figs. 2h and 2i). As mentioned above, the increased number of smaller
649 cloud droplets at the cloud edge facilitate evaporation and results in a lower LWP (Fig. S10). The

larger aerosols from the evaporated clouds return to the accumulation mode, making them more likely to activate as CCN again.

To demonstrate how robust this process on the ACI, we calculate the time series of the ratio of the number concentration of CCN at a supersaturation of 0.2% in the perturbed runs to that in the control runs, normalized by the corresponding accumulation mode aerosol concentration, defined as $(CCN_{0.2\%}/Accu.aerosols)_{perturbed}\Big/(CCN_{0.2\%}/Accu.aerosols)_{control}$, shown in Fig. 10. A ratio greater than 1 suggests that accumulation mode aerosols in the perturbed cases are more readily activated as CCN at a supersaturation of 0.2%, especially in the cases of 20170719 and 20190823. Conversely, a ratio less than 1 is observed during the first half of the day in the 20160701 case, which is attributed to the very low levels of accumulation mode aerosols in the model.

3.4 Cloud liquid water path (LWP) susceptibilities

In this study, the susceptibility of LWP to changes in CCN concentration is quantified using the logarithmic slope between LWP and CCN, denoted as $dln(LWP)/dln(CCN)$ (Gryspeerdt et al., 2019). This slope represents the sensitivity of the LWP in warm stratocumulus clouds to variations in CCN concentration, like shown in Fig. S10c. As presented in Table 2, we aggregate the simulation grids with a spacing resolution of approximately 190 m to form a larger grid of around 25 km for each 10-minute simulation output. This averaging process helps to reduce the impact of heterogeneity and co-variability on the results.

Figure 11 illustrates the averaged cloud susceptibilities for various LWP and CCN or Nc bins across three study periods. The logarithmic slope between LWP and CCN is calculated at each output time (every 10 minutes) using data from 16 aggregated grid points from the control

672 run and 16 aggregated grid points from the perturbed run. Our study reveals that when the CCN
673 concentration is below 100 cm^{-3}, the susceptibility for different LWP and CCN values is positive
674 and the values are large, indicating that changes in LWP are sensitive to variations in CCN number.
675 Here also demonstrates the AIE is large when an increase in CCN can have a large impact on LWP
676 enhancement. However, when the mean CCN concentration exceeds 100 cm^{-3}, the relationship
677 between LWP and CCN becomes more complex, with both positive and negative susceptibilities
678 observed. This suggests that the change in LWP is influenced by other factors, such as
679 environmental conditions and cloud precipitation status. (as shown in Fig. 11a). It is important to
680 note that the CCN number used in our study is averaged from the surface up to the height of 1000
681 m, which may introduce uncertainty to the absolute values of susceptibility by including aerosols
682 that are not directly involved in the aerosol-cloud interaction (Wang et al., 2020).

683 Additionally, our simulations indicate that the Nc in this study is generally low, with a
684 mean value typically below 80 cm^{-3}. For different LWP and Nc values, the susceptibility is mostly
685 positive, indicating that changes in LWP are sensitive to variations in Nc number (as shown in Fig.
686 11c).

687 When we investigate the variation of LWP susceptibility over time, we observe that
688 positive susceptibilities for different LWP and CCN (Nc) typically occur during periods of no rain
689 or light rain (Figs. 12 and S9). On 1 July 2016, the time series of LWP susceptibility for different
690 CCN or Nc shows a diurnal cycle, with large positive values during the nighttime and small
691 positive values in the afternoon. During heavy rain events, such as from 8 to 15 Z local time on
692 19 July 2017 and from 23 Z to 14 Z on 23 August 2019 (Fig. S9), the LWP susceptibilities are
693 negative or close to zero (Figs. 12c and 12e). In the perturbed cases, during the heavy rainfall
694 periods, some aggregated grids show very low LWP (Fig. S10c). This reduction in LWP is caused

by the evaporation from small cloud droplets at non-rain grids on the cloud edge. Those low LWP grids in the perturbed runs result in a negative or near-zero logarithmic slope between LWP and CCN (Figs. S10c, 12c and 12e), although the domain mean LWP is higher in the perturbed case than in the control case (Figs. 9c and 9e).

To further illustrate the reduction in LWP due to evaporation at the cloud edge, Fig. 13 presents the relative change in $ln(LWP)$ between the perturbed and control cases across different LWP percentile ranges in the control case during the periods of negative LWP susceptibility, as shown in Fig. 12. The results indicate a decrease in LWP in the perturbed cases compared to the control cases for pixels with the lowest LWP percentile range (0-25%). We assume that this range corresponds to thin clouds at the edges of the cloud cover.

Figures 11b and 11d display the mean Re susceptibilities for different CCN number and Nc, respectively. The results consistently show that as CCN number or Nc increases, the radius of the cloud droplets decreases. Additionally, the change in Re is more pronounced when Nc (or CCN number) is higher.

In this study, the logarithmic slope between LWP and CCN in the LWP susceptibility calculation is based on a linear assumption. Hoffmann et al. (2024) introduced a heuristic model that represents a significant advancement in understanding the process-level adjustments of cloud water in stratocumulus clouds, suggesting that the relationship may resemble a reversed "V" shape. Figure 13 indicates that the decrease in LWP (negative susceptibilities) in the perturbed cases occurs only in low LWP clouds (thin and non-rain clouds). Conversely, LWP increases (positive susceptibilities) in thicker, precipitating clouds under the perturbed scenarios, which is consistent with the findings of Hoffmann et al. (2024). Since our study aggregates grids to a 25 km resolution, we are able to capture such spatial heterogeneity and retrieve a negative susceptibility due to the

718 evaporation of thin clouds at cloud edge while at 100-km scale (domain-averaged shown in Figs.
719 S11 and S12), the signal is dominated by the increase of LWP at cloud core. However, based on
720 the current study cases, we may not have sufficient data samples to illustrate a relationship beyond
721 the linear assumption.

722 4 Discussion and summary

723 This study focuses on aerosol indirect effects (AIE), particularly involving long-range
724 transport aerosols, in the Eastern North Atlantic (ENA) region. It specifically examines these
725 effects on warm boundary layer stratiform clouds located on the eastern side of oceanic subtropical
726 highs under three different weather regimes: a ridge with a surface high-pressure system, a post-
727 trough with a surface high-pressure system, and a weak trough. We select three specific study
728 cases (i.e., 20160701, 20170719, and 20190823) to assess the impact of long-range transport
729 aerosols on warm boundary layer clouds, with each case representing a typical meteorological
730 regime observed over the ENA site.

731 To investigate aerosol-cloud interactions more realistically, incorporating aerosol
732 chemistry components that activate to cloud condensation nuclei (CCN) and accounting for aerosol
733 spatiotemporal variation, this study employs the Weather Research and Forecast model coupled
734 with a chemistry component (WRF-Chem). This approach provides a detailed examination of AIE
735 in the ENA region under the three specified weather regimes. We employ a downscaling technique
736 to conduct WRF-Chem simulations for the two inner domains (with the outer domains utilizing
737 WRF). This approach results in nearly a 50% reduction in total computational costs, achieving a
738 throughput of 8 hours per day using 1,080 cores.

739 We incorporate major aerosol species (BC, OC, and SO_4), as well as SO_2, from MERRA-
740 2 to provide aerosol initial and boundary conditions, labeled as control cases. Additionally, we

formulate three perturbed cases by amplifying aerosol concentrations in both initial and boundary conditions, as well as sea salt emissions, by a factor of five relative to each control case. Since aerosol features are primarily determined by aerosol initial and boundary conditions, a higher Aiken mode assumption in the major aerosol component (i.e., SO_4) regarding the aerosol mode ratio (80% for Aiken mode and 20% for accumulation mode) results in fewer aerosols activating as CCN due to the curvature effect in our simulations.

The WRF-Chem model captures the cloud structure in the case of 20160701 but underestimates the cloud amount. It simulates the formation of thin, uniform stratocumulus clouds within a meteorological regime characterized by a ridge system in the free troposphere and a high-pressure system near the surface. However, the cases of 20170719 and 20190823 exhibit the development of thicker but broken solid stratocumulus clouds within a post-trough regime and a weak trough, respectively. With the fast-moving cloud systems and strong surface wind, the WRF-Chem model struggles to capture the development and movement of these cloud systems due to delayed moisture transport from outer boundary condition and potential insufficient vertical resolution.

In all cases, compared to the observations, the WRF-Chem model underestimates the liquid water path (LWP) and cloud fraction due to warmer and lower simulated boundary layer. In the perturbed cases, we find 57% higher aerosol-induced LWP, especially for the rain grids. We also note that the perturbed cases exhibit lower rainfall intensity, indicating a rainfall suppression effect attributed to high CCN concentrations as concluded in previous studies (Wang et al., 2020; Christensen et al., 2024). In contrast, the LWP over the non-rain grids only increases by 28%. Moreover, when introducing aerosols in the perturbed runs, the results over the rain grids exhibit larger cloud drops and a wider radius spectrum compared to the results over the non-rain grids.

764 This suggests that the presence of aerosols has a more pronounced effect on cloud properties within
765 the rain grids. The non-rain grids over the cloud edge can have lower LWP because smaller cloud
766 droplets are easy to evaporate.

767 Our study further elucidates the intricate feedback mechanisms governing aerosol-cloud
768 interactions and aerosol properties. In both the post-trough and weak trough regimes, we observe
769 a pronounced tendency for the cloud structure to develop more open-cell stratocumulus clouds.
770 At the peripheries of these clouds, the perturbed cases demonstrate a significant increase in the
771 presence of small cloud droplets. This heightened abundance of smaller droplets promotes
772 evaporation, thereby leading to a marked reduction in LWP.

773 As these clouds evaporate, the aerosols that are released return to the accumulation mode.
774 This transition enhances their likelihood of reactivating as CCN. Consequently, this cycle
775 underscores the dynamic interplay between aerosol properties and cloud formation, highlighting
776 how changes in aerosol concentrations can influence cloud microphysics and, ultimately,
777 precipitation processes.

778 Additionally, the susceptibility of LWP to changes in CCN concentration is quantified
779 using the logarithmic slope between LWP and CCN. Our result shows when the CCN
780 concentration is low, LWP is sensitive to variations in CCN number, with higher CCN number
781 concentration leading to higher LWP. However, when the mean CCN concentration is relatively
782 high, LWP is not as sensitive to changes in CCN, the LWP susceptibilities are small in magnitude,
783 with both positive and negative values. Those negative values are caused by the evaporation from
784 small cloud droplets at non-rain grids on the cloud edge.

785 In Wang et al. (2020), the LWC susceptibility for a light precipitation case on 18 July 2017
786 also shows positive values based on three sensitivity runs with CCN concentrations of 10, 100,

and 1000 cm^{-3}. The cloud properties in their study are averaged over all cloud points in the innermost domain. We adopt the same method as Wang et al. (2020) to estimate the LWP susceptibility using the domain mean values, defined as $\Delta ln(LWP_{perturbed} - LWP_{control})/\Delta ln(CCN_{perturbed} - CCN_{control})$. This approach predominantly yields positive values for LWP susceptibility across the three study cases (see Figs. S11 and S12). This suggests that the 25-km resolution is able to capture such spatial heterogeneity and retrieve a negative susceptibility due to the evaporation of thin clouds at cloud edge while at 100-km scale (domain-averaged), the signal is dominated by the increase of LWP at cloud core.

Conversely, the LWP susceptibilities associated with varying cloud droplet numbers reported in Qiu et al. (2024) reveal significant negative values in LWP susceptibility in response to high cloud droplet numbers, a trend that is partially reflected in our study. Further investigation is required to reconcile the difference in LWP responses between observational data and model simulations. Additionally, a more accurate estimation of LWP susceptibility to changes in CCN concentration is necessary.

Moreover, future research will focus on addressing the identified issues within the model, such as improving the representation of transported aerosol size distributions, resolving the overly fragmented stratocumulus cloud layers with sharp boundary layer inversions, and comparing the modeled cloud susceptibilities with observational data through simulations of ship tracks and local aerosol perturbations.

Code and data availability:

The WRF-Chem code (v4.4.2) used in this study has been released on GitHub (https://github.com/wrf-model/WRF/releases/download/v4.4.2/v4.4.2.tar.gz). The observational data used in this study are available at https://doi.org/10.5281/zenodo.13356995. Other WRF-Chem simulated outputs for the plots in this paper are available at https://doi.org/10.5281/zenodo.13357040.

Author contributions:

H.-H. Lee and X. Zheng provided ideas and designed the experiments in this study. H.-H. Lee conducted all the simulations and analyses. H.-H. Lee leads and coordinates the manuscript with inputs from coauthors.

Competing interests.

At least one of the (co-)authors is a member of the editorial board of Atmospheric Chemistry and Physics.

Acknowledgements:

This work is supported by the DOE Office of Science Early Career Research Program and the ASR Program. Work at LLNL was performed under the auspices of the U.S. DOE by Lawrence Livermore National Laboratory under contract DE-AC52-07NA27344. LLNL IM: LLNL-JRNL-870513.

Reference:

Abdul-Razzak, H. and Ghan, S. J.: A parameterization of aerosol activation: 2. Multiple aerosol types, Journal of Geophysical Research: Atmospheres, 105, 6837-6844, https://doi.org/10.1029/1999JD901161, 2000.

Ackermann, I. J., Hass, H., Memmesheimer, M., Ebel, A., Binkowski, F. S., and Shankar, U.: Modal aerosol dynamics model for Europe: development and first applications, Atmospheric Environment, 32, 2981-2999, http://dx.doi.org/10.1016/S1352-2310(98)00006-5, 1998.

Albrecht, B. A.: Aerosols, Cloud Microphysics, and Fractional Cloudiness, Science, 245, 1227-1230, doi:10.1126/science.245.4923.1227, 1989.

Arola, A., Lipponen, A., Kolmonen, P., Virtanen, T. H., Bellouin, N., Grosvenor, D. P., Gryspeerdt, E., Quaas, J., and Kokkola, H.: Aerosol effects on clouds are concealed by natural cloud heterogeneity and satellite retrieval errors, Nature Communications, 13, 7357, 10.1038/s41467-022-34948-5, 2022.

Binkowski, F. S. and Shankar, U.: The Regional Particulate Matter Model: 1. Model description and preliminary results, Journal of Geophysical Research: Atmospheres, 100, 26191-26209, https://doi.org/10.1029/95JD02093, 1995.

Cadeddu, M. P., Ghate, V. P., and Mech, M.: Ground-based observations of cloud and drizzle liquid water path in stratocumulus clouds, Atmos. Meas. Tech., 13, 1485-1499, 10.5194/amt-13-1485-2020, 2020.

Chapman, E. G., Gustafson Jr, W. I., Easter, R. C., Barnard, J. C., Ghan, S. J., Pekour, M. S., and Fast, J. D.: Coupling aerosol-cloud-radiative processes in the WRF-Chem model: Investigating the radiative impact of elevated point sources, Atmos. Chem. Phys., 9, 945-964, 10.5194/acp-9-945-2009, 2009.

Chen, F. and Dudhia, J.: Coupling an Advanced Land Surface–Hydrology Model with the Penn State–NCAR MM5 Modeling System. Part I: Model Implementation and Sensitivity, Monthly Weather Review, 129, 569-585, https://doi.org/10.1175/1520-0493(2001)129<0569:CAALSH>2.0.CO;2, 2001.

Chen, T., Rossow, W. B., and Zhang, Y.: Radiative Effects of Cloud-Type Variations, Journal of Climate, 13, 264-286, 10.1175/1520-0442(2000)013<0264:Reoctv>2.0.Co;2, 2000.

Chin, M., Ginoux, P., Kinne, S., Torres, O., Holben, B. N., Duncan, B. N., Martin, R. V., Logan, J. A., Higurashi, A., and Nakajima, T.: Tropospheric Aerosol Optical Thickness from the GOCART Model and Comparisons with Satellite and Sun Photometer Measurements, Journal of the Atmospheric Sciences, 59, 461-483, https://doi.org/10.1175/1520-0469(2002)059<0461:TAOTFT>2.0.CO;2, 2002.

Christensen, M. W., Wu, P., Varble, A. C., Xiao, H., and Fast, J. D.: Aerosol-induced closure of marine cloud cells: enhanced effects in the presence of precipitation, Atmos. Chem. Phys., 24, 6455-6476, 10.5194/acp-24-6455-2024, 2024.

Clarke, A. D., Owens, S. R., and Zhou, J.: An ultrafine sea-salt flux from breaking waves: Implications for cloud condensation nuclei in the remote marine atmosphere, Journal of Geophysical Research: Atmospheres, 111, https://doi.org/10.1029/2005JD006565, 2006.

Fast, J. D., Gustafson Jr., W. I., Easter, R. C., Zaveri, R. A., Barnard, J. C., Chapman, E. G., Grell, G. A., and Peckham, S. E.: Evolution of ozone, particulates, and aerosol direct radiative forcing in the vicinity of Houston using a fully coupled meteorology-chemistry-aerosol model, Journal of Geophysical Research: Atmospheres, 111, https://doi.org/10.1029/2005JD006721, 2006.

Feingold, G., Ghate, V. P., Russell, L. M., Blossey, P., Cantrell, W., Christensen, M. W., Diamond, M. S., Gettelman, A., Glassmeier, F., Gryspeerdt, E., Haywood, J., Hoffmann, F., Kaul, C. M., Lebsock, M., McComiskey, A. C., McCoy, D. T., Ming, Y., Mülmenstädt, J., Possner, A., Prabhakaran, P., Quinn, P. K., Schmidt, K. S., Shaw, R. A., Singer, C. E., Sorooshian, A., Toll, V., Wan, J. S., Wood, R., Yang, F., Zhang, J., and Zheng, X.: Physical science research needed to evaluate the viability and risks of marine cloud brightening, Science Advances, 10, eadi8594, doi:10.1126/sciadv.adi8594, 2024.

Gallo, F., Uin, J., Sanchez, K. J., Moore, R. H., Wang, J., Wood, R., Mei, F., Flynn, C., Springston, S., Azevedo, E. B., Kuang, C., and Aiken, A. C.: Long-range transported continental aerosol in the eastern North Atlantic: three multiday event regimes influence cloud condensation nuclei, Atmos. Chem. Phys., 23, 4221-4246, 10.5194/acp-23-4221-2023, 2023.

Ghate, V. P. and Cadeddu, M. P.: Drizzle and Turbulence Below Closed Cellular Marine Stratocumulus Clouds, Journal of Geophysical Research: Atmospheres, 124, 5724-5737, https://doi.org/10.1029/2018JD030141, 2019.

Ghate, V. P., Surleta, T., Magaritz-Ronen, L., Raveh-Rubin, S., Gallo, F., Carlton, A. G., and Azevedo, E. B.: Drivers of Cloud Condensation Nuclei in the Eastern North Atlantic as Observed at the ARM Site, Journal of Geophysical Research: Atmospheres, 128, e2023JD038636, https://doi.org/10.1029/2023JD038636, 2023.

Gong, S. L.: A parameterization of sea-salt aerosol source function for sub- and super-micron particles, Global Biogeochemical Cycles, 17, https://doi.org/10.1029/2003GB002079, 2003.

Grell, G. A., Peckham, S. E., Schmitz, R., McKeen, S. A., Frost, G., Skamarock, W. C., and Eder, B.: Fully coupled “online” chemistry within the WRF model, Atmospheric Environment, 39, 6957-6975, https://doi.org/10.1016/j.atmosenv.2005.04.027, 2005.

Gryspeerdt, E., Goren, T., Sourdeval, O., Quaas, J., Mülmenstädt, J., Dipu, S., Unglaub, C., Gettelman, A., and Christensen, M.: Constraining the aerosol influence on cloud liquid water path, Atmos. Chem. Phys., 19, 5331-5347, 10.5194/acp-19-5331-2019, 2019.

Hartmann, D. L., Ockert-Bell, M. E., and Michelsen, M. L.: The Effect of Cloud Type on Earth's Energy Balance: Global Analysis, Journal of Climate, 5, 1281-1304, 10.1175/1520-0442(1992)005<1281:Teocto>2.0.Co;2, 1992.

Hersbach, H., Bell, B., Berrisford, P., Biavati, G., Horányi, A., Muñoz Sabater, J., Nicolas, J., Peubey, C., Radu, R., Rozum, I., Schepers, D., Simmons, A., Soci, C., Dee, D., and Thépaut, J.-N.: ERA5 hourly data on single levels from 1940 to present. Copernicus Climate Change Service (C3S) Climate Data Store (CDS) [dataset], 10.24381/cds.adbb2d47 2023.

Hoffmann, F., Glassmeier, F., and Feingold, G.: The impact of aerosol on cloud water: a heuristic perspective, Atmos. Chem. Phys., 24, 13403-13412, 10.5194/acp-24-13403-2024, 2024.

913 Hong, S.-Y. and Jang, J.: Impacts of Shallow Convection Processes on a Simulated Boreal
914 Summer Climatology in a Global Atmospheric Model, Asia-Pacific Journal of Atmospheric
915 Sciences, 54, 361-370, 10.1007/s13143-018-0013-3, 2018.
916 Iacono, M. J., Delamere, J. S., Mlawer, E. J., Shephard, M. W., Clough, S. A., and Collins, W.
917 D.: Radiative forcing by long-lived greenhouse gases: Calculations with the AER radiative
918 transfer models, Journal of Geophysical Research: Atmospheres, 113,
919 10.1029/2008jd009944, 2008.
920 Janjić, Z. I.: The Step-Mountain Eta Coordinate Model: Further Developments of the
921 Convection, Viscous Sublayer, and Turbulence Closure Schemes, Monthly Weather
922 Review, 122, 927-945, https://doi.org/10.1175/1520-
923 0493(1994)122<0927:TSMECM>2.0.CO;2, 1994.
924 kazemirad, M. and Miller, M. A.: Summertime Post-Cold-Frontal Marine Stratocumulus
925 Transition Processes over the Eastern North Atlantic, Journal of the Atmospheric Sciences,
926 77, 2011-2037, https://doi.org/10.1175/JAS-D-19-0167.1, 2020.
927 Kazil, J., Wang, H., Feingold, G., Clarke, A. D., Snider, J. R., and Bandy, A. R.: Modeling
928 chemical and aerosol processes in the transition from closed to open cells during
929 VOCALS-REx, Atmos. Chem. Phys., 11, 7491-7514, 10.5194/acp-11-7491-2011, 2011.
930 Klein, S. A. and Hartmann, D. L.: The Seasonal Cycle of Low Stratiform Clouds, Journal of
931 Climate, 6, 1587-1606, 10.1175/1520-0442(1993)006<1587:Tscols>2.0.Co;2, 1993.
932 Knievel, J. C., Bryan, G. H., and Hacker, J. P.: Explicit Numerical Diffusion in the WRF
933 Model, Monthly Weather Review, 135, 3808-3824,
934 https://doi.org/10.1175/2007MWR2100.1, 2007.
935 Lee, S. S., Donner, L. J., Phillips, V. T. J., and Ming, Y.: The dependence of aerosol effects on
936 clouds and precipitation on cloud-system organization, shear and stability, Journal of
937 Geophysical Research: Atmospheres, 113, https://doi.org/10.1029/2007JD009224, 2008.
938 Liljegren, J. C., Clothiaux, E. E., Mace, G. G., Kato, S., and Dong, X.: A new retrieval for
939 cloud liquid water path using a ground-based microwave radiometer and measurements of
940 cloud temperature, Journal of Geophysical Research: Atmospheres, 106, 14485-14500,
941 https://doi.org/10.1029/2000JD900817, 2001.
942 Liu, X., Easter, R. C., Ghan, S. J., Zaveri, R., Rasch, P., Shi, X., Lamarque, J. F., Gettelman,
943 A., Morrison, H., Vitt, F., Conley, A., Park, S., Neale, R., Hannay, C., Ekman, A. M. L., Hess,
944 P., Mahowald, N., Collins, W., Iacono, M. J., Bretherton, C. S., Flanner, M. G., and Mitchell,
945 D.: Toward a minimal representation of aerosols in climate models: description and
946 evaluation in the Community Atmosphere Model CAM5, Geosci. Model Dev., 5, 709-739,
947 10.5194/gmd-5-709-2012, 2012.
948 Logan, T., Xi, B., and Dong, X.: Aerosol properties and their influences on marine boundary
949 layer cloud condensation nuclei at the ARM mobile facility over the Azores, Journal of
950 Geophysical Research: Atmospheres, 119, 4859-4872,
951 https://doi.org/10.1002/2013JD021288, 2014.
952 Mather, J. H. and Voyles, J. W.: The Arm Climate Research Facility: A Review of Structure
953 and Capabilities, Bulletin of the American Meteorological Society, 94, 377-392,
954 https://doi.org/10.1175/BAMS-D-11-00218.1, 2013.
955 McCoy, I. L., Wyant, M. C., Blossey, P. N., Bretherton, C. S., and Wood, R.: Aitken Mode
956 Aerosols Buffer Decoupled Mid-Latitude Boundary Layer Clouds Against Precipitation

Depletion, Journal of Geophysical Research: Atmospheres, 129, e2023JD039572, https://doi.org/10.1029/2023JD039572, 2024.
Mechem, D. B., Wittman, C. S., Miller, M. A., Yuter, S. E., and de Szoeke, S. P.: Joint Synoptic and Cloud Variability over the Northeast Atlantic near the Azores, Journal of Applied Meteorology and Climatology, 57, 1273-1290, https://doi.org/10.1175/JAMC-D-17-0211.1, 2018.
Mellor, G. L. and Yamada, T.: Development of a turbulence closure model for geophysical fluid problems, Reviews of Geophysics, 20, 851-875, https://doi.org/10.1029/RG020i004p00851, 1982.
Minnis, P., Sun-Mack, S., Young, D. F., Heck, P. W., Garber, D. P., Chen, Y., Spangenberg, D. A., Arduini, R. F., Trepte, Q. Z., Smith, W. L., Ayers, J. K., Gibson, S. C., Miller, W. F., Hong, G., Chakrapani, V., Takano, Y., Liou, K. N., Xie, Y., and Yang, P.: CERES Edition-2 Cloud Property Retrievals Using TRMM VIRS and Terra and Aqua MODIS Data—Part I: Algorithms, IEEE Transactions on Geoscience and Remote Sensing, 49, 4374-4400, 10.1109/TGRS.2011.2144601, 2011.
Minnis, P., Sun-Mack, S., Chen, Y., Chang, F. L., Yost, C. R., Smith, W. L., Heck, P. W., Arduini, R. F., Bedka, S. T., Yi, Y., Hong, G., Jin, Z., Painemal, D., Palikonda, R., Scarino, B. R., Spangenberg, D. A., Smith, R. A., Trepte, Q. Z., Yang, P., and Xie, Y.: CERES MODIS Cloud Product Retrievals for Edition 4—Part I: Algorithm Changes, IEEE Transactions on Geoscience and Remote Sensing, 59, 2744-2780, 10.1109/TGRS.2020.3008866, 2021.
Mlawer, E. J., Taubman, S. J., Brown, P. D., Iacono, M. J., and Clough, S. A.: Radiative transfer for inhomogeneous atmospheres: RRTM, a validated correlated-k model for the longwave, Journal of Geophysical Research: Atmospheres, 102, 16663-16682, https://doi.org/10.1029/97JD00237, 1997.
Modeling, G. and Office, A.: MERRA-2 inst3_3d_aer_Nv: 3d, 3-hourly, instantaneous, model-level, assimilation, aerosol mixing ratio V5. 12.4, 2015.
Molod, A., Takacs, L., Suarez, M., and Bacmeister, J.: Development of the GEOS-5 atmospheric general circulation model: evolution from MERRA to MERRA2, Geosci. Model Dev., 8, 1339-1356, 10.5194/gmd-8-1339-2015, 2015.
Monin, A. S. and Obukhov, A. M.: Basic laws of turulent mixing in the atmosphere near the ground, Tr. Inst. Teor. Geofiz. Akad. Nauk SSSR, 24, 1963-1987, 1954.
Morrison, H., Thompson, G., and Tatarskii, V.: Impact of Cloud Microphysics on the Development of Trailing Stratiform Precipitation in a Simulated Squall Line: Comparison of One- and Two-Moment Schemes, Monthly Weather Review, 137, 991-1007, https://doi.org/10.1175/2008MWR2556.1, 2009.
Painemal, D., Spangenberg, D., Smith Jr, W. L., Minnis, P., Cairns, B., Moore, R. H., Crosbie, E., Robinson, C., Thornhill, K. L., Winstead, E. L., and Ziemba, L.: Evaluation of satellite retrievals of liquid clouds from the GOES-13 imager and MODIS over the midlatitude North Atlantic during the NAAMES campaign, Atmos. Meas. Tech., 14, 6633-6646, 10.5194/amt-14-6633-2021, 2021.
Qiu, S., Zheng, X., Painemal, D., Terai, C. R., and Zhou, X.: Daytime variation in the aerosol indirect effect for warm marine boundary layer clouds in the eastern North Atlantic, Atmos. Chem. Phys., 24, 2913-2935, 10.5194/acp-24-2913-2024, 2024.

Rémillard, J. and Tselioudis, G.: Cloud Regime Variability over the Azores and Its Application to Climate Model Evaluation, Journal of Climate, 28, 9707-9720, https://doi.org/10.1175/JCLI-D-15-0066.1, 2015.
Schell, B., Ackermann, I. J., Hass, H., Binkowski, F. S., and Ebel, A.: Modeling the formation of secondary organic aerosol within a comprehensive air quality model system, Journal of Geophysical Research: Atmospheres (1984–2012), 106, 28275-28293, 2001.
Skamarock, W., Klemp, J., Dudhia, J., Gill, D., Liu, Z., Berner, J., and Huang, X.: A description of the advanced research WRF model version 4.3 (No. NCAR/TN-556+ STR).[Software], 2021.
Skamarock, W. C., Klemp, J. B., Dudhia, J., Gill, D. O., Barker, D. M., Duda, M. G., Huang, X.-Y., Wang, W., and Powers, J. G.: A description of the advanced research WRF version 3, NCAR technical note, 475, 10.5065, 2008.
Stephens, G. L. and Greenwald, T. J.: The Earth's radiation budget and its relation to atmospheric hydrology: 2. Observations of cloud effects, Journal of Geophysical Research: Atmospheres, 96, 15325-15340, 10.1029/91jd00972, 1991.
Stockwell, W. R., Kirchner, F., Kuhn, M., and Seefeld, S.: A new mechanism for regional atmospheric chemistry modeling, Journal of Geophysical Research: Atmospheres, 102, 25847-25879, 10.1029/97JD00849, 1997.
Terai, C. R., Bretherton, C. S., Wood, R., and Painter, G.: Aircraft observations of aerosol, cloud, precipitation, and boundary layer properties in pockets of open cells over the southeast Pacific, Atmos. Chem. Phys., 14, 8071-8088, 10.5194/acp-14-8071-2014, 2014.
Tian, J., Dong, X., Xi, B., Williams, C. R., and Wu, P.: Estimation of liquid water path below the melting layer in stratiform precipitation systems using radar measurements during MC3E, Atmos. Meas. Tech., 12, 3743-3759, 10.5194/amt-12-3743-2019, 2019.
Toon, O. B., Kasting, J. F., Turco, R. P., and Liu, M. S.: The sulfur cycle in the marine atmosphere, Journal of Geophysical Research: Atmospheres, 92, 943-963, https://doi.org/10.1029/JD092iD01p00943, 1987.
Tuccella, P., Curci, G., Visconti, G., Bessagnet, B., Menut, L., and Park, R. J.: Modeling of gas and aerosol with WRF/Chem over Europe: Evaluation and sensitivity study, Journal of Geophysical Research: Atmospheres, 117, https://doi.org/10.1029/2011JD016302, 2012.
Twomey, S.: Pollution and the planetary albedo, Atmospheric Environment (1967), 8, 1251-1256, https://doi.org/10.1016/0004-6981(74)90004-3, 1974.
Twomey, S.: Aerosols, clouds and radiation, Atmospheric Environment. Part A. General Topics, 25, 2435-2442, https://doi.org/10.1016/0960-1686(91)90159-5, 1991.
Wang, J., Wood, R., Jensen, M. P., Chiu, J. C., Liu, Y., Lamer, K., Desai, N., Giangrande, S. E., Knopf, D. A., Kollias, P., Laskin, A., Liu, X., Lu, C., Mechem, D., Mei, F., Starzec, M., Tomlinson, J., Wang, Y., Yum, S. S., Zheng, G., Aiken, A. C., Azevedo, E. B., Blanchard, Y., China, S., Dong, X., Gallo, F., Gao, S., Ghate, V. P., Glienke, S., Goldberger, L., Hardin, J. C., Kuang, C., Luke, E. P., Matthews, A. A., Miller, M. A., Moffet, R., Pekour, M., Schmid, B., Sedlacek, A. J., Shaw, R. A., Shilling, J. E., Sullivan, A., Suski, K., Veghte, D. P., Weber, R., Wyant, M., Yeom, J., Zawadowicz, M., and Zhang, Z.: Aerosol and Cloud Experiments in the Eastern North Atlantic (ACE-ENA), Bulletin of the American Meteorological Society, 103, E619-E641, https://doi.org/10.1175/BAMS-D-19-0220.1, 2022.

Wang, Y., Zheng, X., Dong, X., Xi, B., Wu, P., Logan, T., and Yung, Y. L.: Impacts of long-range transport of aerosols on marine-boundary-layer clouds in the eastern North Atlantic, Atmos. Chem. Phys., 20, 14741-14755, 10.5194/acp-20-14741-2020, 2020.
Warren, S. G., Hahn, C. J., London, J., Chervin, R. M., Jenne, R. L., Colorado Univ., B., CO . Cooperative Inst. for Research in Environmental Sciences, Colorado Univ., B., CO . Dept. of Astrophysical, Planetary,, Sciences, A., and National Center for Atmospheric Research, B., CO): Global distribution of total cloud cover and cloud type amounts over the ocean, United States, Medium: ED; Size: Pages: (305 p), 10.2172/5415329, 1988.
Wood, R.: Stratocumulus Clouds, Monthly Weather Review, 140, 2373-2423, 10.1175/mwr-d-11-00121.1, 2012.
Wood, R., Wyant, M., Bretherton, C. S., Rémillard, J., Kollias, P., Fletcher, J., Stemmler, J., de Szoeke, S., Yuter, S., Miller, M., Mechem, D., Tselioudis, G., Chiu, J. C., Mann, J. A. L., O'Connor, E. J., Hogan, R. J., Dong, X., Miller, M., Ghate, V., Jefferson, A., Min, Q., Minnis, P., Palikonda, R., Albrecht, B., Luke, E., Hannay, C., and Lin, Y.: Clouds, Aerosols, and Precipitation in the Marine Boundary Layer: An Arm Mobile Facility Deployment, Bulletin of the American Meteorological Society, 96, 419-440, https://doi.org/10.1175/BAMS-D-13-00180.1, 2015.
Zaveri, R. A., Barnard, J. C., Easter, R. C., Riemer, N., and West, M.: Particle-resolved simulation of aerosol size, composition, mixing state, and the associated optical and cloud condensation nuclei activation properties in an evolving urban plume, Journal of Geophysical Research: Atmospheres, 115, https://doi.org/10.1029/2009JD013616, 2010.
Zhang, H., DeNero, S. P., Joe, D. K., Lee, H. H., Chen, S. H., Michalakes, J., and Kleeman, M. J.: Development of a source oriented version of the WRF/Chem model and its application to the California regional PM₁₀ / PM_{2.5} air quality study, Atmos. Chem. Phys., 14, 485-503, 10.5194/acp-14-485-2014, 2014.
Zhang, Z., Song, Q., Mechem, D. B., Larson, V. E., Wang, J., Liu, Y., Witte, M. K., Dong, X., and Wu, P.: Vertical dependence of horizontal variation of cloud microphysics: observations from the ACE-ENA field campaign and implications for warm-rain simulation in climate models, Atmos. Chem. Phys., 21, 3103-3121, 10.5194/acp-21-3103-2021, 2021.
Zheng, Q. and Miller, M. A.: Summertime Marine Boundary Layer Cloud, Thermodynamic, and Drizzle Morphology over the Eastern North Atlantic: A Four-Year Study, Journal of Climate, 35, 4805-4825, https://doi.org/10.1175/JCLI-D-21-0568.1, 2022.
Zheng, X., Dong, X., Xi, B., Logan, T., and Wang, Y.: Distinctive aerosol-cloud-precipitation interactions in marine boundary layer clouds from the ACE-ENA and SOCRATES aircraft field campaigns, EGUsphere, 2023, 1-45, 10.5194/egusphere-2023-2608, 2023.
Zheng, X., Xi, B., Dong, X., Wu, P., Logan, T., and Wang, Y.: Environmental effects on aerosol–cloud interaction in non-precipitating marine boundary layer (MBL) clouds over the eastern North Atlantic, Atmos. Chem. Phys., 22, 335-354, 10.5194/acp-22-335-2022, 2022.
Zheng, X., Qiu, S., Zhang, D., Adebiyi, A. A., Zheng, X., Faruque, O., Tao, C., and Wang, J.: Variability of Eastern North Atlantic Summertime Marine Boundary Layer Clouds and Aerosols Across Different Synoptic Regimes Identified with Multiple Conditions, ESS Open Archive, 10.22541/essoar.172434363.30466798/v1, 2024.

Zheng, Y., Zhu, Y., Rosenfeld, D., and Li, Z.: Climatology of Cloud-Top Radiative Cooling in Marine Shallow Clouds, Geophysical Research Letters, 48, e2021GL094676, https://doi.org/10.1029/2021GL094676, 2021.
Zhou, X. and Feingold, G.: Impacts of Mesoscale Cloud Organization on Aerosol-Induced Cloud Water Adjustment and Cloud Brightness, Geophysical Research Letters, 50, e2023GL103417, https://doi.org/10.1029/2023GL103417, 2023.

Table 1. WRF physics scheme configuration

Physics Processes	Scheme	Reference
Microphysics	Morrison (2 moments) scheme	Morrison et al. (2009)
Longwave radiation	RRTMG scheme	Mlawer et al. (1997)
Shortwave radiation	RRTMG scheme	Iacono et al. (2008)
Surface-layer	Monin-Obukhov surface layer	Monin and Obukhov (1954)
Land surface	Unified Noah land-surface model	Chen and Dudhia (2001)
Planetary boundary layer	MYJ (Eta) TKE scheme (d01 and d02 only)	Mellor and Yamada (1982) Janjić (1994)
Shallow cumulus parameterization	GRIMS scheme (d01 and d02 only)	Hong and Jang (2018)

Table 2. Ten-minute mean and standard deviation of cloud condensation nuclei (CCN), liquid water path (LWP), cloud droplet number (Nc), cloud radius (Re), and rainfall intensity (RI) over three study cases. Data are averaged over ~25 km of the domain 4 and total 16 averaged grids are in the domain 4. Rain and non-rain are averaged the grids when the RI on the grid is larger than and equal to zero, respectively. Only CCN are averaged within 1000 m height over the domain 4, other variables are averaged within 2000 m height.

Area	Case	CCN (cm^{-3})	LWP ($g\ m^{-2}$)	Nc (cm^{-3})	Re (μm)	RI ($mm\ hr^{-1}$)
Domain	Control	73.07 ± 48.77	53.17 ± 32.65	22.68 ± 11.59	9.97 ± 2.31	0.009 ± 0.033
	Perturbed	286.88 ± 183.69 (+293%)	79.25 ± 56.62 (+49%)	59.74 ± 27.29 (+163%)	7.83 ± 2.02 (-21%)	0.008 ± 0.033 (-11%)
Rain	Control	68.15 ± 48.05	58.57 ± 31.69	20.17 ± 9.33	10.47 ± 2.07	0.011 ± 0.035
	Perturbed	250.14 ± 153.23 (+267%)	91.81 ± 55.06 (+57%)	53.01 ± 20.39 (+163%)	8.35 ± 1.83 (-20%)	0.009 ± 0.036 (-18%)
Non-Rain	Control	103.73 ± 41.52	18.91 ± 9.81	38.57 ± 11.93	6.81 ± 0.76	0 ± 0
	Perturbed	444.47 ± 217.08 (+328%)	24.22 ± 15.80 (+28%)	89.24 ± 33.42 (+131%)	5.54 ± 0.90 (-19%)	0 ± 0

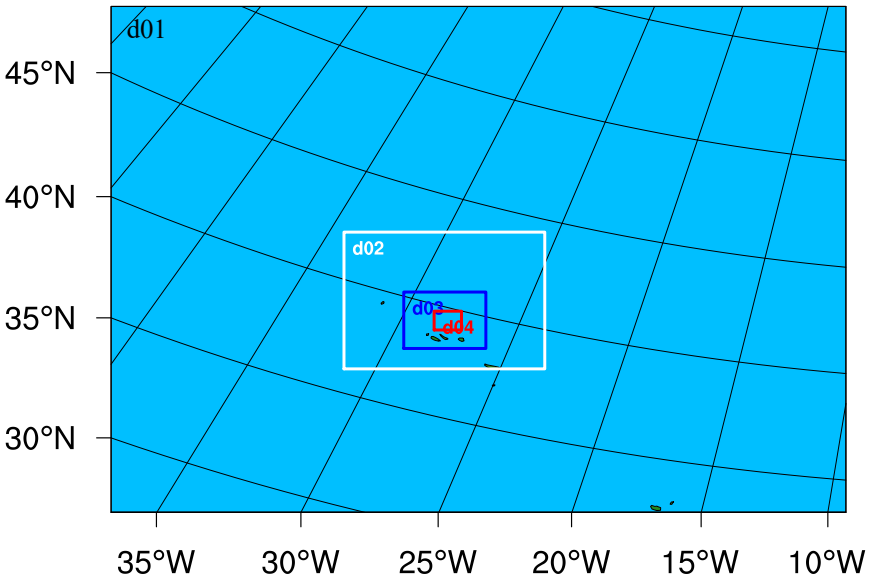

Figure 1. Model domains are designed for simulations. The 4 domains denote 4 horizontal resolutions of 5 km (d01), 1.67 km (d02), 0.56 km (d03), and 0.19 km (d04), respectively.

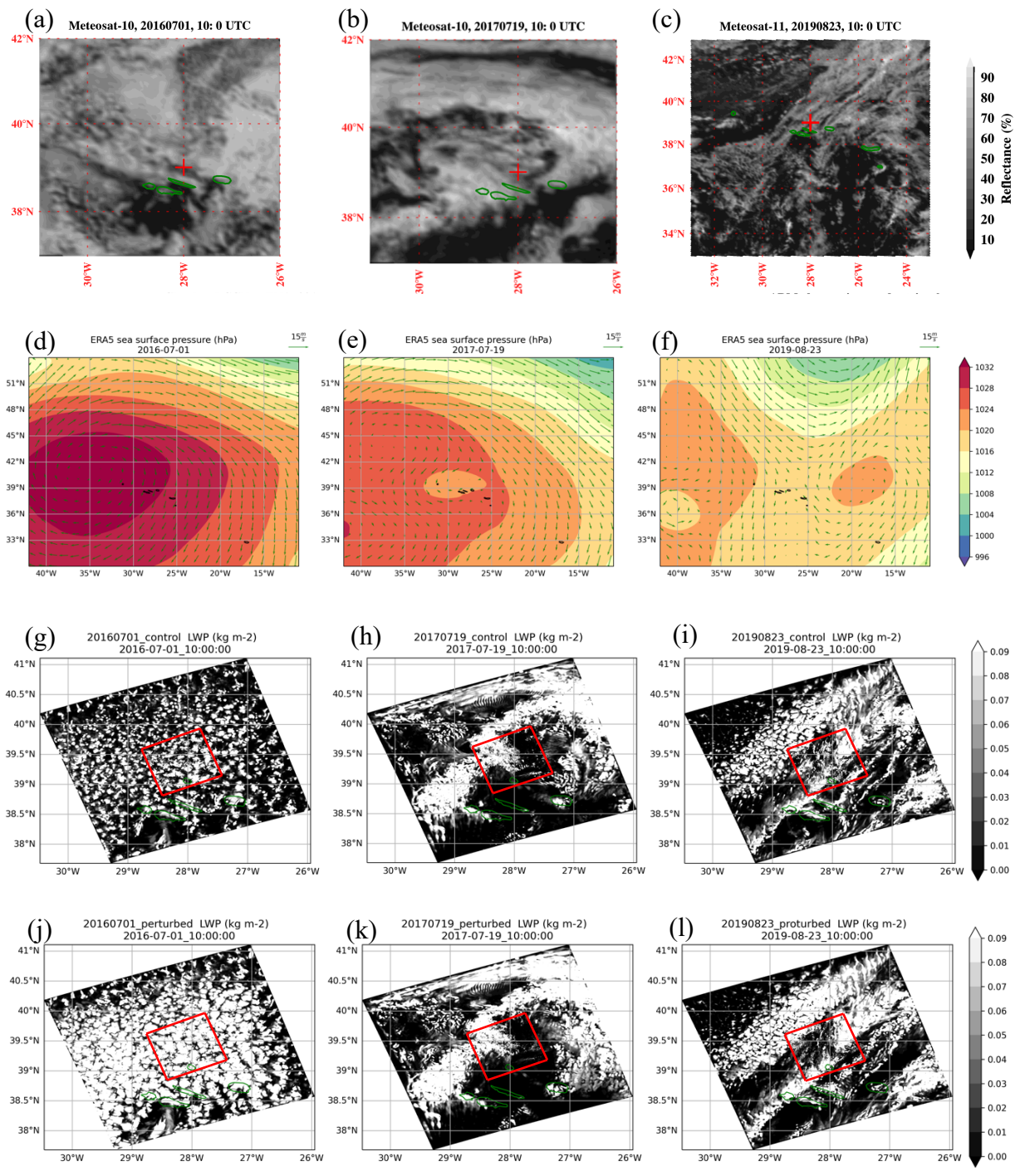

Figure 2. Spinning Enhanced Visible Infra-Red Imager (SEVIRI) images from the Meteosat satellite at 10:00 UTC on (a) 1 July 2016, (b) 19 July 2017, and (c) 23 August 2019 over the ENA. (d), (e), and (f) are on the same day of (a), (b), and (c), respectively, but from the ERA5 mean sea surface pressure (contour; units: hPa) and 10-meter surface wind (arrow; units: m s^{-1}). (g), (h), and (i) are on the same day of (a), (b), and (c), respectively, but from the WRF-Chem

simulated liquid water path (LWP; units: kg m^{-2}) in the control runs, while (j), (k), and (l) are in the perturbed runs. The red boxes in the figures indicate the result from domain 4.

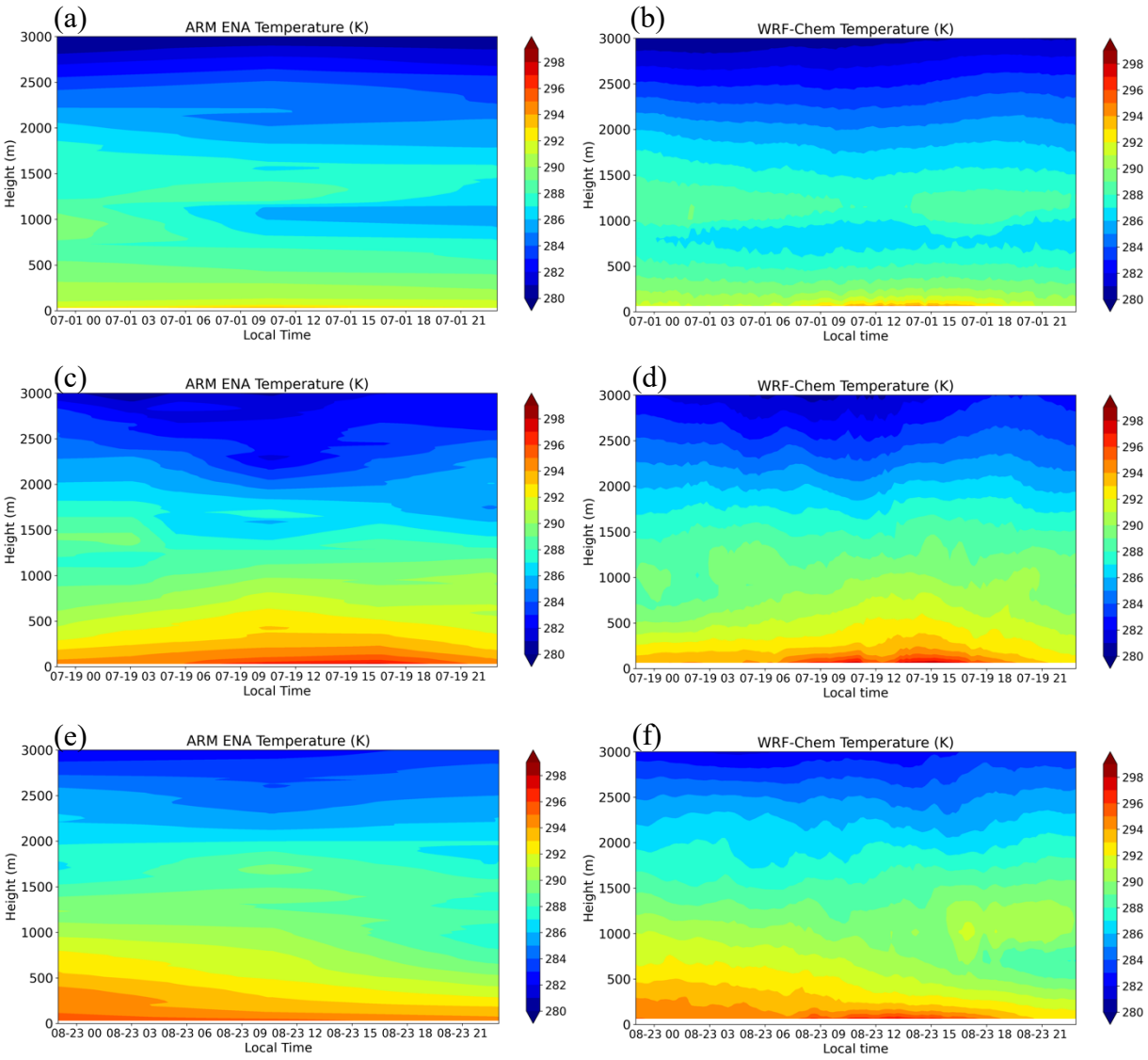

Figure 3. The time series (local time; UTC -1 hour) of temperature profiles (units: K) from ARM interpolated soundings at the Azores (39.09°N, -28.02°W) on (a) 1 July 2016, (c) 19 July 2017, and (e) 23 August 2019. Panels (b), (d), and (f) depict the same dates as (a), (c), and (e), respectively, but show the average temperature from WRF-Chem simulated results over 20 × 20 grids centered on the Azores (approximately 4 km resolution).

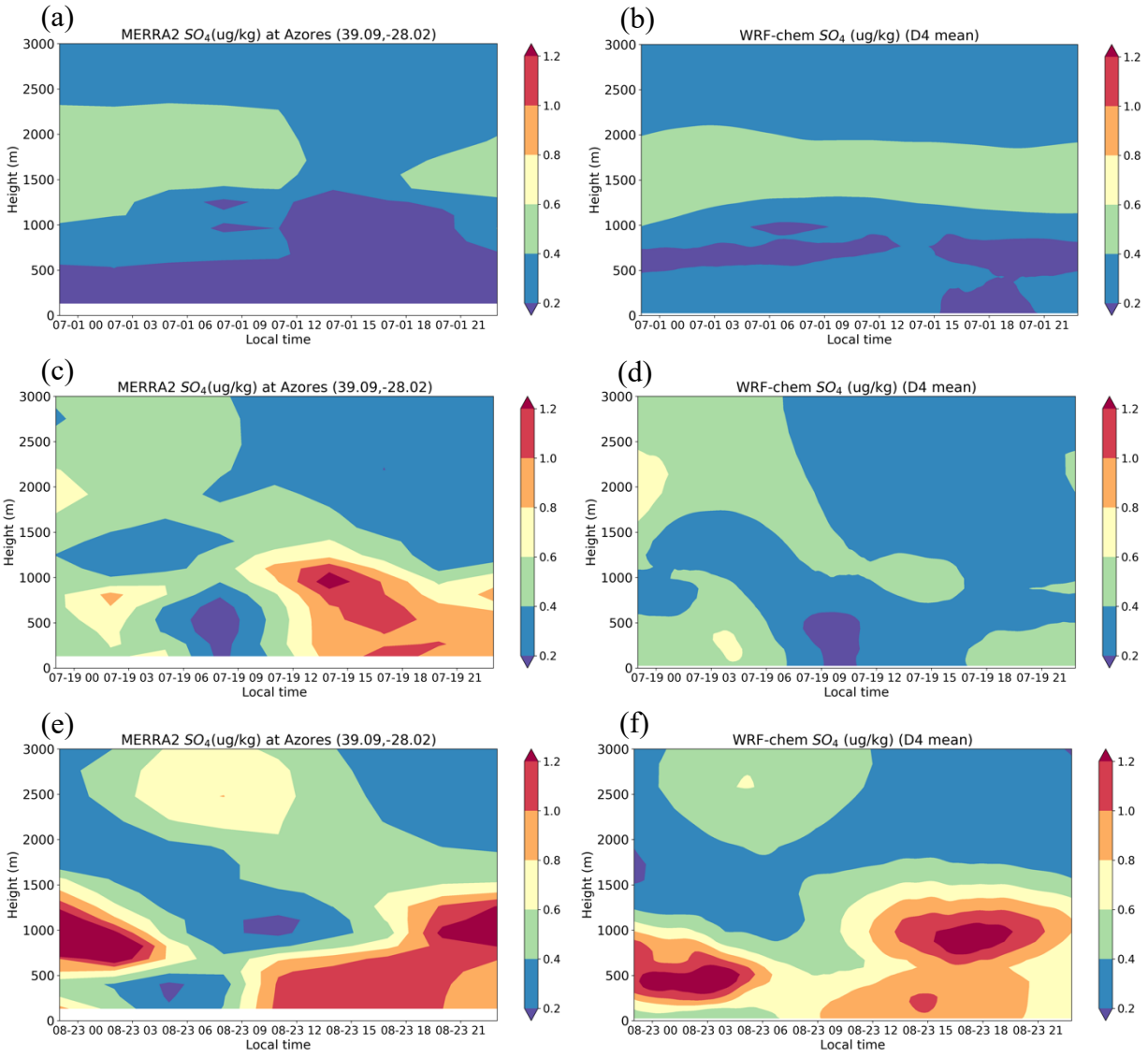

Figure 4. The time series (local time; UTC – 1 hour) of SO_4 profiles (units: μg kg^{-1}) from MERRA-2 at the Azores (39.09°N, -28.02°W) on (a) 1 July 2016, (c) 19 July 2017, and (e) 23 August 2019. Panels (b), (d), and (f) depict the same dates as (a), (c), and (e), respectively, but show the average aerosol concentration from WRF-Chem simulated data over domain 4.

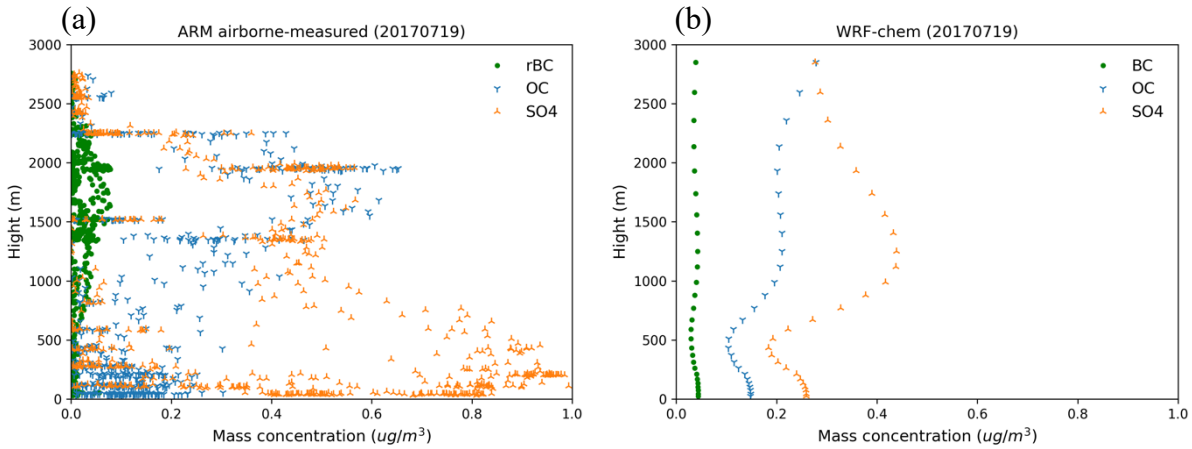

Figure 5. (a) ARM airborne-measured vertical profiles of SO_4, OC and refractory BC (rBC) mass concentration (units: μg cm^{-3}) averaged over multiple flights on 19 July 2017. Note that the highly uncertain and noisy aerosol observations between 600 – 1000 m height due to cloud contamination. (b) WRF-Chem simulated vertical profile of SO_4, OC, and BC mass concentration (units: μg cm^{-3}) averaged over domain 4 during the flight time from 8:40 to 11:50 UTC.

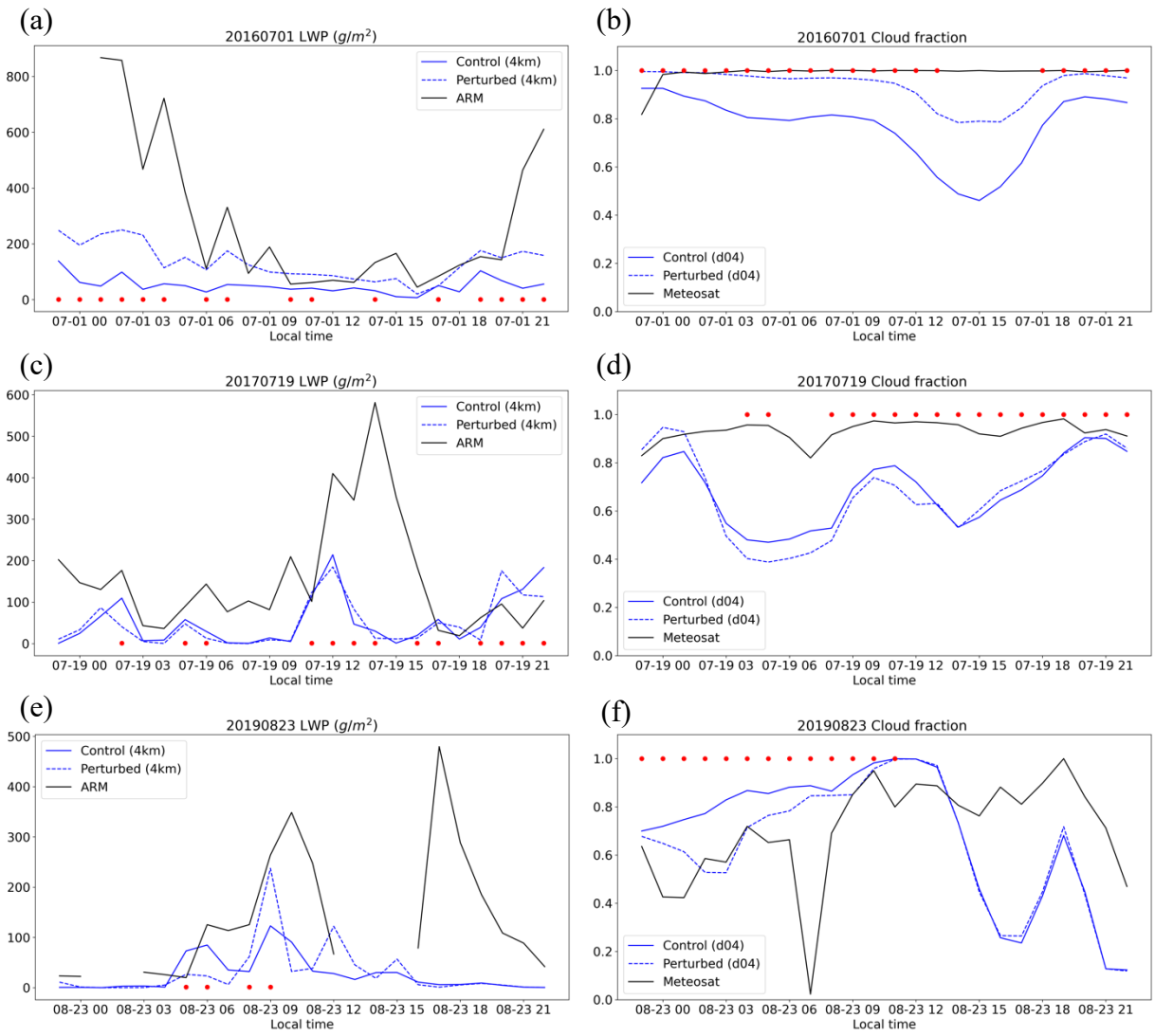

Figure 6. (a), (c), and (e) are the hourly time series (local time; UTC - 1 hour) of 4 km-averaged (4km) liquid water path (units: g m^{-2}) simulated from WRF-Chem (blue solid line) and observed from ARM (black solid line) on 1 July 2016, 19 July 2017, and 23 August 2019, respectively. (b), (d), and (f) are the hourly time series of domain-averaged (d04) cloud fraction simulated from WRF-Chem (blue solid line) and observaed from Meteosat (black solid line) on 1 July 2016, 19 July 2017, and 23 August 2019, respectively. The 4 km-averaged data are averaged from the model simulated results over 20 × 20 grids centered on the Azores (approximately 4 km resolution). The red dots indicate when rainfall intensity is higher than 0.001 (0.01) mm hr^{-1} in 4-km averaged area (domain 4).

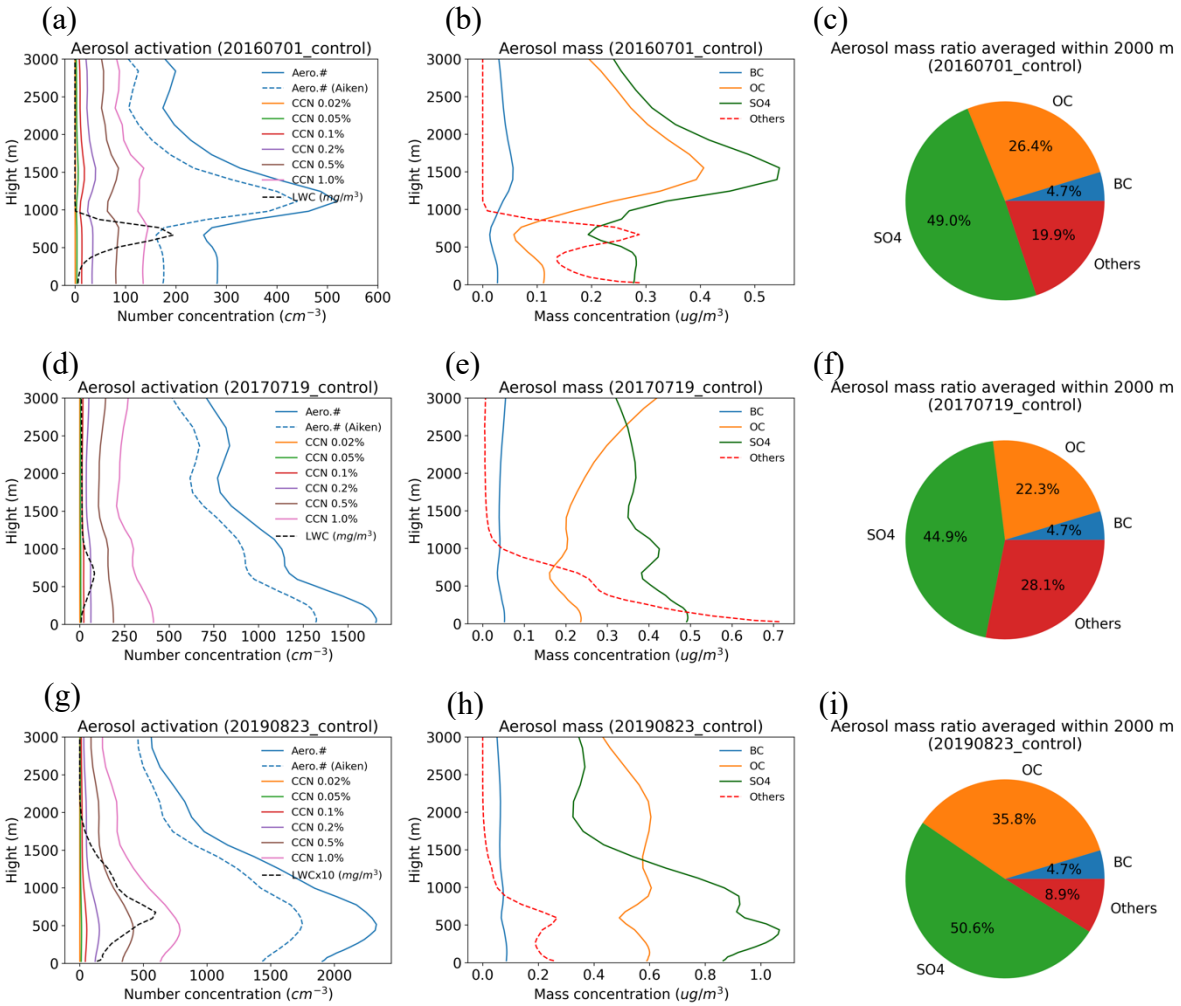

Figure 7. (a), (d), and (g) WRF-Chem vertical profiles of aerosol number concentration (Aiken mode and accumulation mode; units: cm^{-3}), aerosol number concentration (Aiken mode only; units: cm^{-3}), CCN number concentration below different supersaturations (units: cm^{-3}), and liquid water content (cloud and rain; units: mg m^{-3}) averaged over the domain 4 on 1 July 2016, 19 July 2017, and 23 August 2019, respectively, in the control runs. (b), (e), and (h) WRF-Chem vertical profiles of BC, OC, SO_4, and other species (like sea salt) (units: μg cm^{-3}) averaged over the domain 4 on 1 July 2016, 19 July 2017, and 23 August 2019, respectively, in the control runs. (c), (f), and (i) Pie chart of aerosol mass of different species averaged within 2000 m height on 1 July 2016, 19 July 2017, and 23 August 2019, respectively, in the control runs. Note that LWC is adjusted to fit the scale of x-axis for each case.

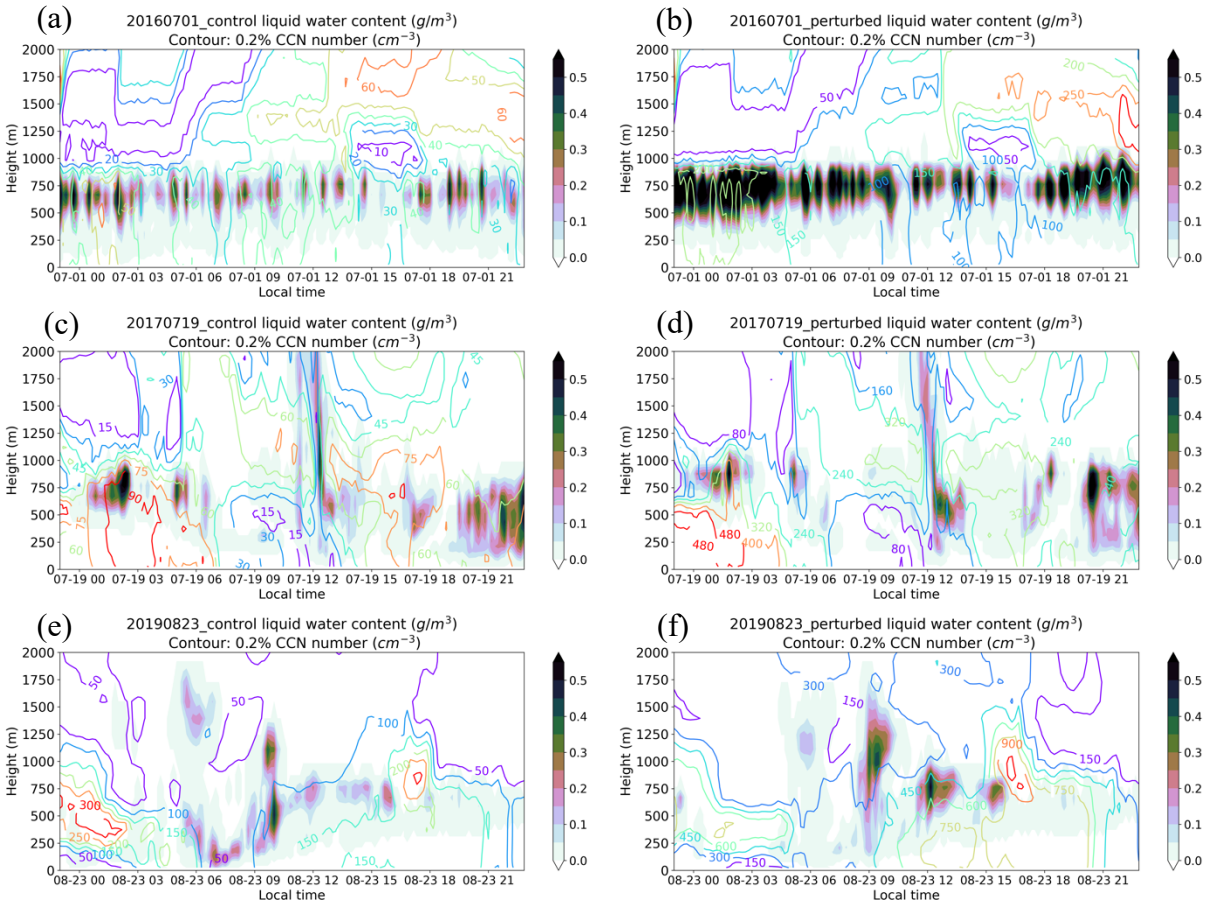

Figure 8. (a), (c), and (e) are the time series (local time; UTC – 1 hour) of 4 km-averaged cloud liquid water content profile (shade; units: g cm^{-3}) and CCN (0.2% supersaturation) number concentration profile (contour; units: # cm^{-3}) on 1 July 2016, 19 July 2017, and 23 August 2019, respectively, in the control runs. (b), (d), and (f) are the same as (a), (c), and (e), respectively, but in the perturbed runs. The data are averaged from the model simulated results over 20 × 20 grids centered on the Azores (approximately 4 km resolution).

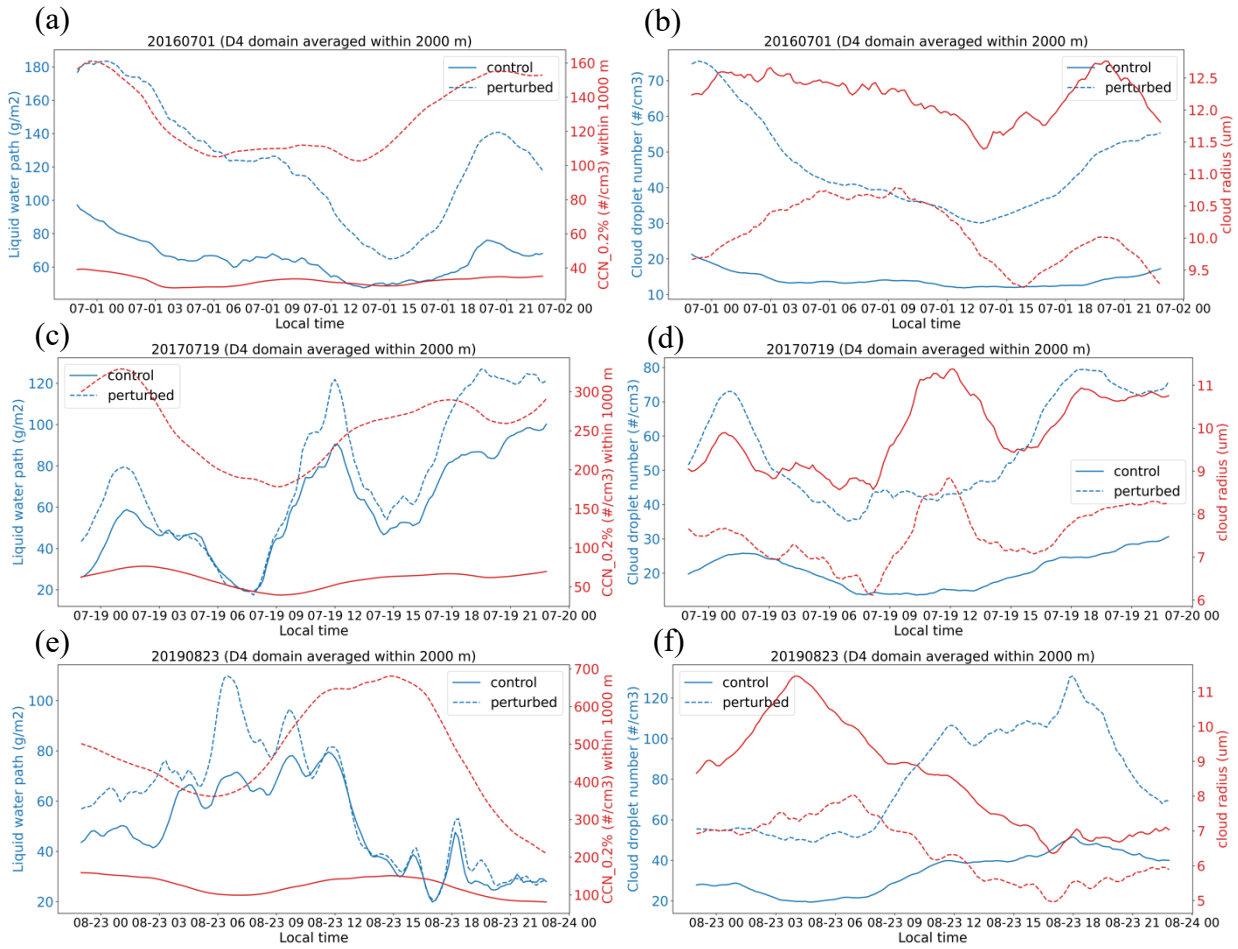

Figure 9. (a), (c), and (e) are the time series of domain-averaged liquid water path (blue lines; units: g m^{-2}) and CCN number concentration below 0.2% supersaturation (red lines; units: # cm^{-2}) for the control case (soild lines) and the perturbed case (dashed lines) on 1 July 2016, 19 July 2017, and 23 August 2019, respectively. (b), (d), and (f) are the time series of domain-averaged cloud droplet number (blue lines; units: # cm^{-3}) and cloud radius (red lines; units: μm) for the control (soild lines) and perturbed (dashed lines) on 1 July 2016, 19 July 2017, and 23 August 2019, respectively. Only CCN data are averaged within 1000 m height over domain 4, other variables are averaged within 2000 m height.

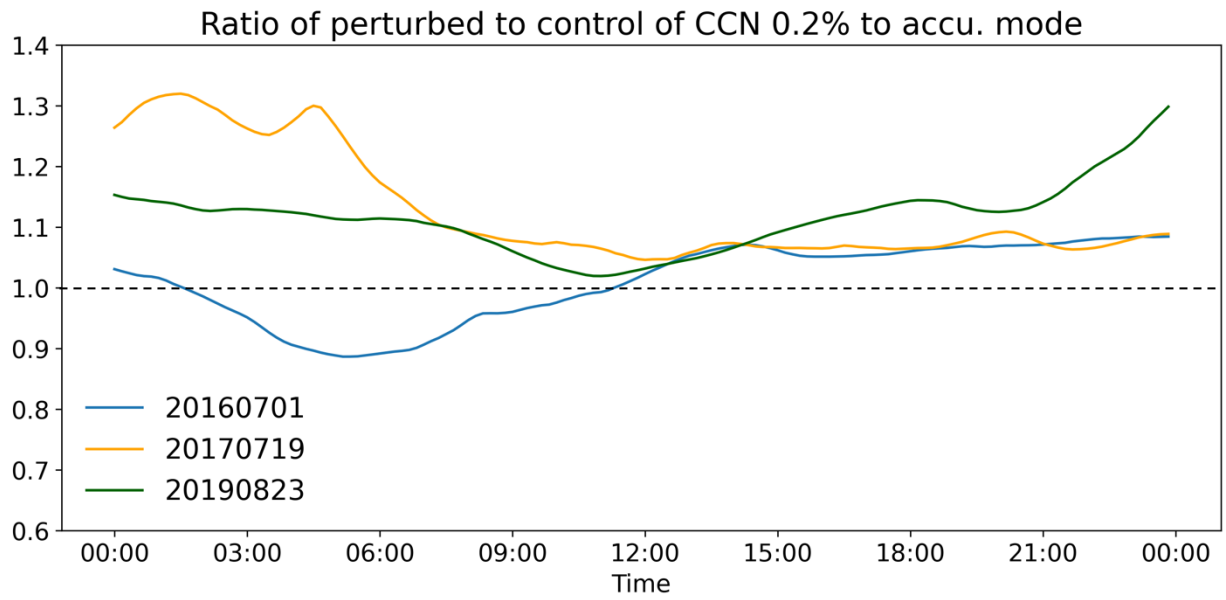

Figure 10. The time series of the ratio of the number concentration of CCN at a supersaturation of 0.2% in the perturbed runs to that in the control runs, normalized by the corresponding accumulation mode aerosol concentration, defined as $(CCN_{0.2\%}/Accu.aerosols)_{perturbed} \Big/ (CCN_{0.2\%}/Accu.aerosols)_{control}$. The black dashed line indicates the value of unity.

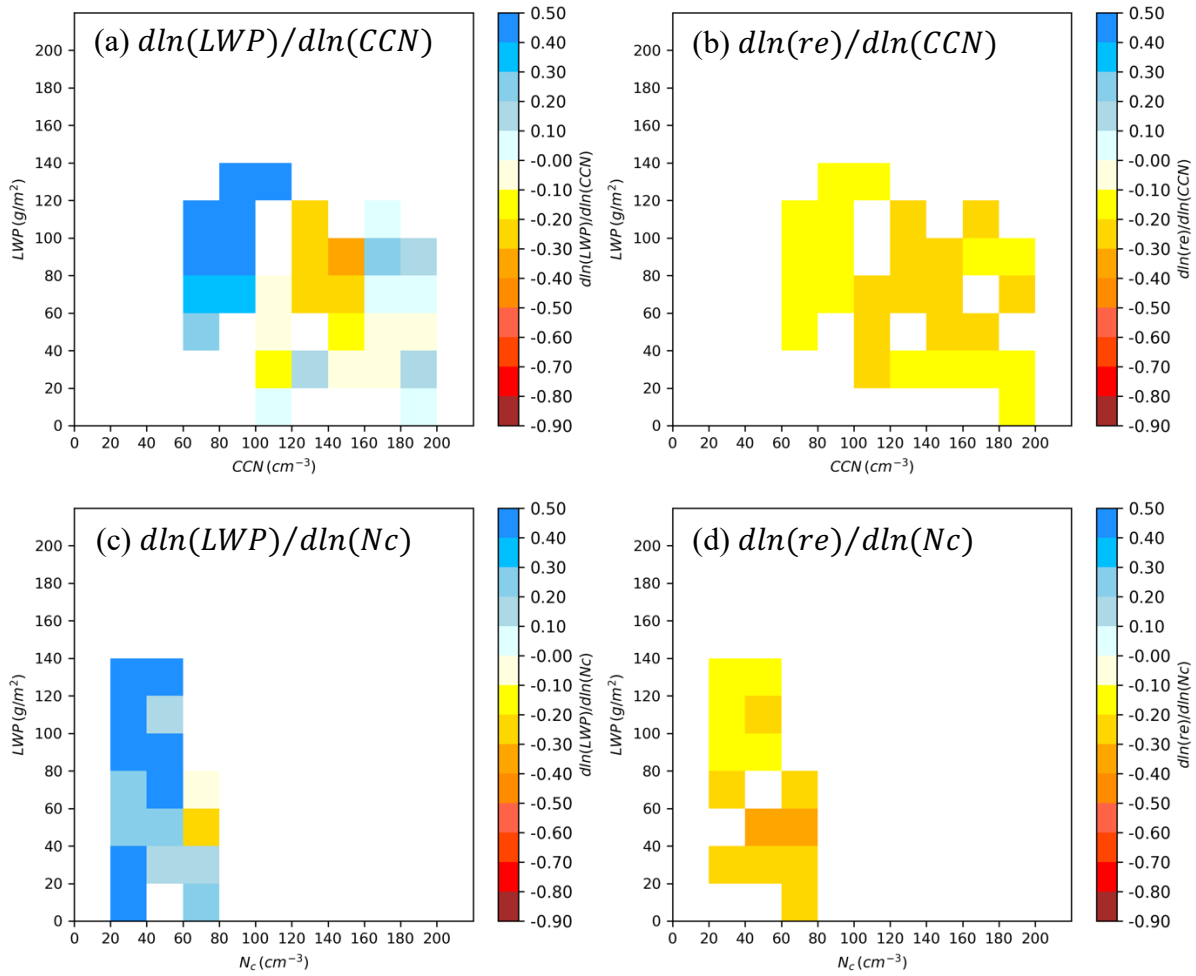

Figure 11. (a) and (b) are the mean liquid water path (LWP) and cloud radius (Re) susceptibilities for different cloud condensation nuclei (CCN) and LWP bins for three study cases, respectively. (c) and (d) are the same as (a) and (b), respectively, but for different cloud droplet number (Nc) and LWP bins. The logarithmic slope between LWP and CCN, denoted as ($dln(LWP)/dln(CCN)$), is calculated at each output time (every 10 minutes) using data from 16 aggregate grid points (~25 km for each grid point) from the control run and 16 aggregated grid points from the perturbed run.

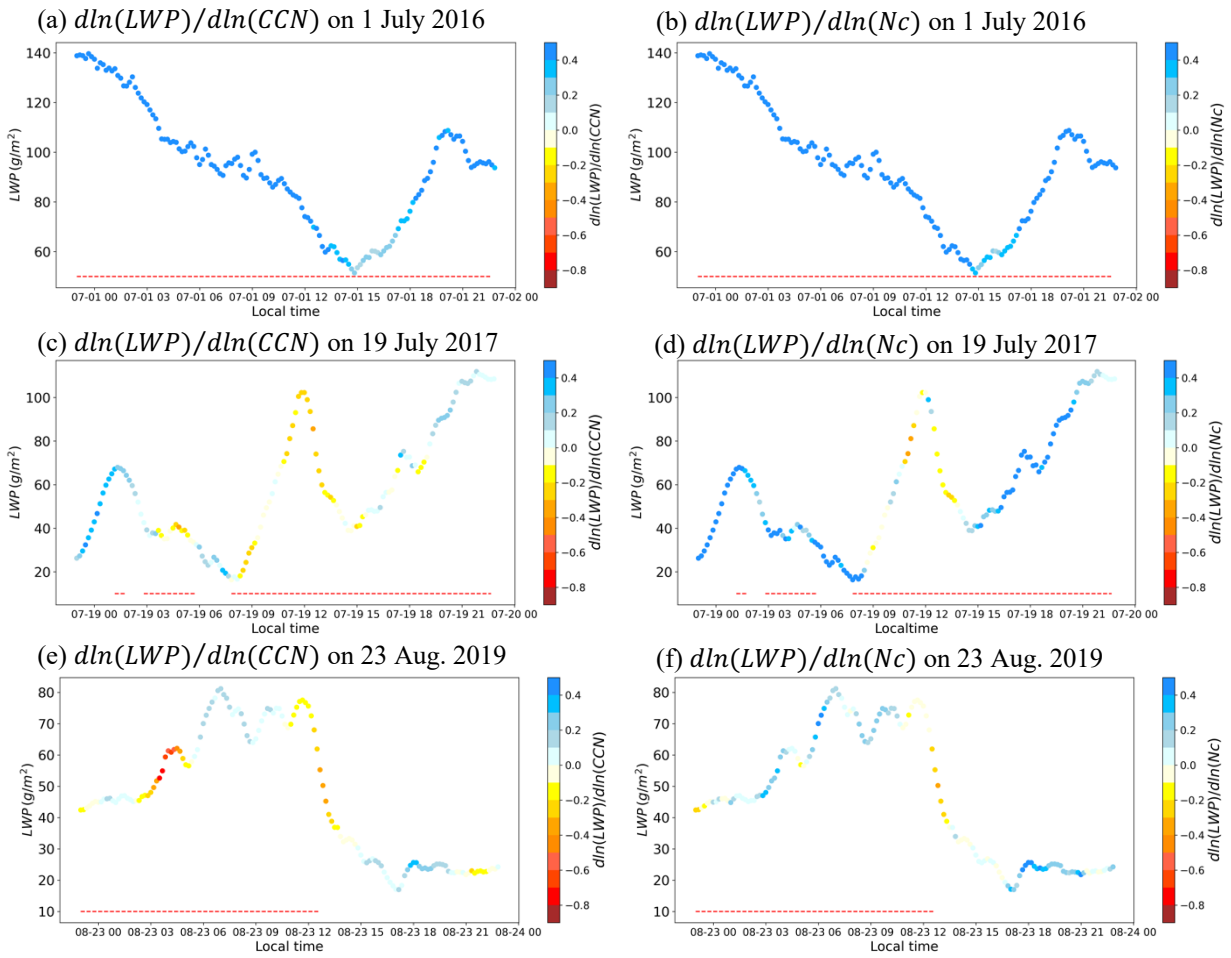

Figure 12. (a), (c) and (e) are the time variable of LWP susceptibility for different CCN concentration, denoted as $(dln(LWP)/dln(CCN))$, on 1 July 2016, 19 July 2017, and 23 August 2019, respectively. (b), (d) and (f) are the time variable of LWP susceptibility for different Nc concentration, denoted as $(dln(LWP)/dln(Nc))$, on 1 July 2016, 19 July 2017, and 23 August 2019, respectively. The logarithmic slope between LWP and CCN is calculated at each output time (every 10 minutes) using data from 16 aggregate grid points (~25 km for each grid point) from the control run and 16 aggregated grid points from the perturbed run. The red dished lines indicate when rainfall intensity is higher than 0.001 mm 10-min^{-1} in domain 4.

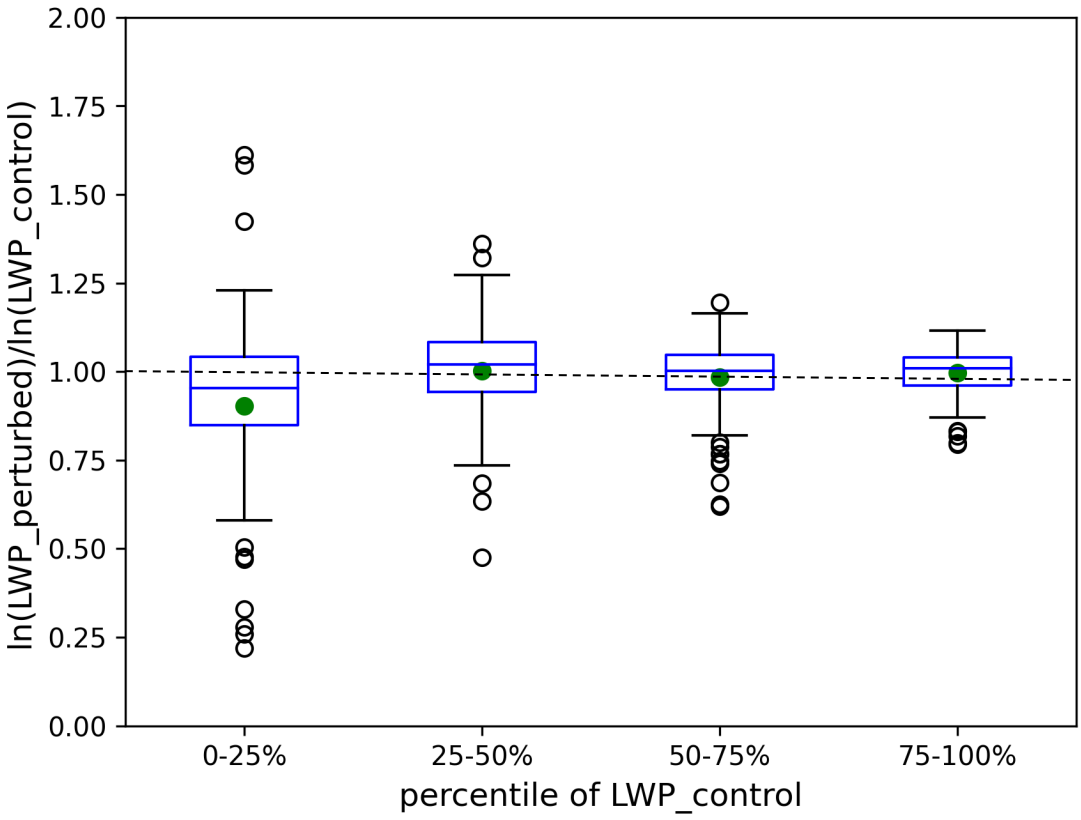

Figure 13. Boxplot of the relative change in $ln(LWP)$ between the perturbed and control cases across different LWP Percentile rages in the control case during the negative susceptibility for LWP shown in Fig. 12. The box extends from the first quartile to the third quartile of the data, with a line at the median. The whiskers extend from the box to the farthest data point lying within 1.5x the inter-quartile range from the box. Outlier values are those past the end of the whiskers. Green dots are the mean value, and the back dashed line indicates the value of 1.0.